Measuring the Nonlinear Optical Properties of Monolayer Tungsten Disulfide with Optically-Pumped Atomic Force Microscopy

Josephine Spiegelberg, Department of Physics

McGill University, Montreal

July, 2022

A thesis submitted to McGill University in partial fulfillment of the requirements of the degree of

Master of Science

Abstract

Spatially resolving the optical nonlinearity of a material can be important for understanding the role of defects in its optical and electronic properties. This is particularly interesting for two-dimensional transition metal dichalcogenides, which represent a new class of materials with a large nonlinear optical susceptibility and a wide variety of applications, especially for small scale optoelectronics.

In this work, we first use an optically-pumped, frequency modulated atomic force microscope (AFM) to measure the second order nonlinear optical susceptibility ($\chi^{(2)}$) of the merocyanide dye HB238. Measurements on this molecule, known to have a large dipole moment, were used primarily to better understand the origin of the AFM signal. The amplitude of a mechanically measured optical autocorrelation was found to vary quadratically with power, confirming that the signal originates from nonlinear optical effects within the material. In addition, the noise in the AFM was found to increase dramatically at time delays close to zero and vary approximately quadratically with power.

The second half of this work describes efforts to produce and characterize monolayers of WS_2. Samples were manufactured through both mechanical exfoliation and chemical vapor deposition (CVD) and characterized using amplitude modulated AFM in air. The CVD-grown flakes were found to have oxidized but displayed interesting light-dependent, long-term charge storage behaviors.

Abrégé

La résolution spatiale de la non-linéarité optique d'un matériel peut être importante pour comprendre le rôle des défauts dans ses propriétés optiques et électroniques. Ceci est particulièrement intéressant pour les dichalcogénures de métaux de transition bidimensionnels, ce qui représente une nouvelle classe de matériaux avec une grande susceptibilité optique non-linéaire et une variété large d'applications, surtout pour les optoélectroniques à petite échelle.

Dans ce travail, nous utilisons d'abord un microscope à force atomique (MFA) à fréquence modulée et à pompage optique afin de mesurer la susceptibilité optique non-linéaire de deuxième ordre, ($\chi^{(2)}$), du colorant merocyanure HB238. Les mesures sur cette molécule, qui est connue pour avoir un grand moment dipolaire, ont été utilisées principalement pour mieux comprendre l'origine du signal du MFA. L'amplitude d'une autocorrélation optique mesurée mécaniquement a été observée à varier quadratiquement avec la puissance, ce qui confirme que le signal est originaire d'effets optiques non-linéaires du matériel. De plus, il a été constaté que le bruit du MFA augmentait considérablement à des délais quasi-zéro et variait approximativement quadratiquement avec la puissance.

La deuxième moitié de ce travail décrit les efforts à produire et à caractériser les monocouches de WS_2. Les échantillons ont été manufacturés à travers l'exfoliation mécanique ainsi que le dépôt chimique en phase vapeur (CVD), et ont été caractérisés à l'aide du MFA modulé en amplitude à l'air. Les flocons cultivés se sont oxydés, mais ont néanmoins présenté des comportements de stockage intéressants long-terme dépendant de la lumière.

Acknowledgements

Firstly, I would thank my supervisor Peter Grütter for giving me the opportunity to work on this exciting project in a wonderful environment. I would not have gotten far without his unwavering optimism and support, and I am so thankful for the introduction in to the rich world of AFM and condensed matter in general.

I also want to thank all of the people who shaped my time in Montreal and at McGill. From Megan, for teaching me everything she knows about the JEOL system and really making me feel at home in the Wong basement, to Catherine and Ahmad for always being willing to listen to my troubleshooting complaints and for ensuring that the office is a place I look forward to going, to Logan and George for going through this Masters journey with me, from Covid shutdowns to writing together at Thompson house. Thank you also to the whole Grütter group for always being willing to lend a helping hand or some words of encouragement when I needed them. I will miss our group lunches, not just for the scientific talks but also for the great company. Finally, thank you to my friends from Friday club and beyond for making Montreal feel like home. I am lucky to have found people and a place that make saying goodbye so hard.

Lastly, I want to thank my parents for always supporting me and believing me. I love you and I would not be where I am today without you.

Table of Contents

Chapter 1

Background and Theory

1.1 Transition Metal Dichalcogenides

In 2004, Novoselov et al. published the first paper describing few-layer graphitic films, called graphene, which displayed new and exciting electrical properties [1]. Since then, graphene has been the focus on much research, and many have hoped to find applications in electronics and more. However, though it displays very high carrier mobility, graphene's lack of a band gap means that graphene-based transistors have low on/off switching ratios and, therefore, poses a barrier to the development of graphene-based electronics. Nonetheless, graphene has opened to door to the development and study of many other two-dimensional materials including hexagonal boron nitride (h-BN), 2D boron (borophene), 2D silicon (silicene), 2D germanium (germanene), and 2D transition metal dichalcogenides, which are the focus of this project [2].

Transition metal dichalcogenides, often abbreviated as TMDCs, are materials with the chemical formula MX_2, where M is a transition metal sandwiched between two atomic layers of a chalcogen, X [3]. These layered materials are held together by weak van der Waals interlayer forces. In many cases, a single layer is defined as an X-M-X arrangement in the z-direction, as shown in Figure 1.1 [4].

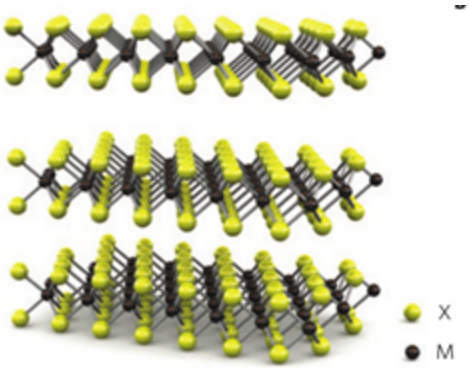

Figure 1.1: Transition metal dichalcogenides with a chemical formula MX_2 display a layered structure with a chalcogen-metal-chalcogen structure. Figure adapted from [4].

Weak interlayer forces mean that TMDCs are easily isolated into few- and single-layer samples, which exhibit a variety of interesting layer-dependent properties. One example of such a phenomenon is the bandgap of semiconducting TMDCs. Most semiconducting TMDCs display a transition from an indirect bandgap to a higher energy direct bandgap in the visible to near-IR range when going from the bulk material to a single layer. This includes some of the most common TMDCs: MoS_2, $MoSe_2$, $MoTe_2$, WSe_2, and WS_2 [3]. The direct bandgap in these monolayer TMDCs has many potential applications for low-dimensional lasers, LEDs, photovoltaics, optical switches, photodetectors, and more [3]. It also allows them to overcome the on/off switching problem found in graphene transistors.

In addition, while bulk TMDCs display inversion symmetry as shown in Figure 1.1, monolayer TMDCs are noncentrosymmetric. For example, bulk MoS_2 belongs to the D_{6h} symmetry group while monolayers have D_{3h} symmetry [5]. This lack of inversion symmetry in monolayers leads to a variety of interesting properties, especially in group-IV semiconducting dichalcogenides (MoS_2, $MoSe_2$, WS_2, and WSe_2). This group of materials have high elemental masses, which, in combination with the lack of inversion symmetry and in-plane confinement of electron motion in monolayers, leads to a strong spin-orbit splitting and spin-valley coupling [4]. These properties are not only interesting for

studying fundamental physics, but they also have promising applications for spintronic devices.

The lack of inversion symmetry in monolayer MX_2 TMDs also results in a large nonlinear optical response. This makes them potential candidates for a wide variety of nonlinear optical applications such as parametric amplification, signal modulation, and terahertz generation [6]. The nonlinear optical properties of these materials will be the main focus of this work.

In addition to their lack of inversion symmetry, monolayer TMDCs exhibit a variety of unique electrical and physical properties that lead to many potential applications. For example, because they have few dangling bonds, these materials have very high mobilities, comparable to those found in silicon [3]. This, in combination with their relatively large direct bandgap, makes them promising materials for building very small transistors. They are also inherently thin, giving them a high surface-to-volume ratio, which is particularly useful for designing sensors as well as improved transistors with reduced power dissipation and good switching control [4]. In addition, there is no significant lattice mismatch between the monolayers, so they can be easily stacked to create heterojunctions with good band-alignment, tunneling transports, and strong inter-layer coupling for LEDs, photodetectors, tunneling transistors, and other applications. Finally, their structural stability and high Young's modulus means that monolayer TMDCs can survive the strain of being mounted on flexible substrates to create cutting edge flexible electronics [3].

Of course, it is also important to note that in addition to their wide variety of potential applications, these materials are also interesting from a fundamental physics perspective. For one, they exhibit strong exciton binding energies, which allows for the study of exciton dynamics at room temperature [7]. In addition, their band structure displays strong splitting of the valence band at the K and K' points. In other words, at these points the valence band displays two maxima with slightly different energies [8]. This strong spin-orbit splitting of the electronic bands in combination with spin-valley coupling leads to

a lot of unique phenomena [4,7]. For example, it has been shown in MoS_2 that the split valence band is spin-polarized, so that electrons in different valleys, or energy band extrema, can be addressed by exciting with circularly polarized light [4,8]. Transition metal dichalcogenides are interesting both for investigating new scientific phenomena and for a wide variety of potential applications.

1.2 Nonlinear Optics Overview

Among the many unique properties of monolayer MX_2 TMDCs, their noncentrosymmetric structure is particularly interesting, as it leads to a strong nonlinear optical response. Typically, this response is characterized by the second- or third-order non-linear optical susceptibility, which describe the electrical polarization of a material in response to the presence of an applied optical field. This induced polarization can be particularly useful as a tool for characterizing these materials using an AFM, as will be discussed in Section 1.4. Thus, a brief overview of optical nonlinear effects and nonlinear susceptibilities will follow.

In traditional linear optics, the polarization, P, of a material is linearly related to the applied electrical field, E, by the linear susceptibility $\chi^{(1)}$ and the permittivity of free space ϵ_0 such that

$$\widetilde{P}(t) = \epsilon_0 \chi^{(1)} \widetilde{E}(t), \tag{1.1}$$

where the tilde denotes a quantity varying rapidly with time [9]. This expression for the polarization can be expanded as a power series in field strength as

$$\widetilde{P}(t) = \epsilon_0 [\chi^{(1)} \widetilde{E}(t) + \chi^{(2)} \widetilde{E}^2(t) + \chi^{(3)} \widetilde{E}^3(t) + \ldots], \tag{1.2}$$

where $\chi^{(2)}$ and $\chi^{(3)}$ are the second- and third- order nonlinear susceptibilities (assumed to be wavelength independent for now) and $\widetilde{P}(t)$ and $\widetilde{E}(t)$ are written as scalars for simplicity. The higher order terms $\epsilon_0 \chi^{(2)} \widetilde{E}^2(t) = \widetilde{P}^{(2)}(t)$ and $\epsilon_0 \chi^{(3)} \widetilde{E}^3(t) = \widetilde{P}^{(3)}(t)$ are no longer

linearly dependent on the incident field intensity and are therefore known as the second- and third-order nonlinear polarization, respectively. Thus, the second-order nonlinear susceptibility $\chi^{(2)}$ which is of interest in this experiment, describes the second-order term of the polarization induced by an optical field.

A more rigorous description of the second-order nonlinear susceptibility and its physical consequences will now be presented, following Boyd's Nonlinear Optics [9].

First, let us assume that the electric field vector of the incident optical wave can be represented as a discrete sum of frequency components,

$$\widetilde{E}(r,t) = \sum_{n'} \widetilde{E}_n(r,t), \tag{1.3}$$

where the sum over n' indicates a summation over only positive frequencies, and the electric field oscillates at a frequency ω_n such that,

$$\widetilde{E}_n(r,t) = E(r,\omega_n)\, e^{-i\omega_n t} + c.c.. \tag{1.4}$$

Now, asserting that,

$$E(r,-\omega_n) = E(r,\omega_n)^*, \tag{1.5}$$

the total field can be written compactly as

$$\widetilde{E}(r,t) = \sum_{n} E(r,\omega_n)\, e^{-i\omega_n t}, \tag{1.6}$$

where the sum is now over all frequencies.

The polarization of the material can similarly be expanded as a sum of various frequency components such that

$$\widetilde{P}(r,t) = \sum_{n} P(r,\omega_n)\, e^{-i\omega_n t}. \tag{1.7}$$

As mentioned above, the polarization can be thought of as a power series with a first-order linear polarization as well as second- and third-order nonlinear terms. Focusing on the second-order non-linear polarization, one can define the constants of proportionality relating the product of the amplitudes of the three-dimensional field and the nonlinear polarization as the components of a second-order susceptibility tensor (rather than a scalar second-order susceptibility). Then, the i$^{\text{th}}$ component of the second-order nonlinear polarization becomes

$$P_i\left(\omega_n+\omega_m\right)=\epsilon_0\sum_{jk}\sum_{(nm)}\chi^{(2)}_{ijk}\left(\omega_n+\omega_m,\omega_n,\omega_m\right)E_j\left(\omega_n\right)E_k\left(\omega_m\right), \tag{1.8}$$

where i, j, and k indicate the Cartesian components of the fields and polarization, (nm) indicates a summation over n and m where the sum $\omega_n+\omega_m$ remains constant but the individual frequencies are allowed to vary. As per Equation 1.6, each field amplitude $E\left(\omega_{n/m}\right)$ contains a time dependence $e^{-i\omega_{n/m}t}$ such that their product (and the resulting polarization) has a time dependence of $e^{-i(\omega_n+\omega_m)t}$ oscillating at frequency $(\omega_n+\omega_m)$.

The indices n and m in Equation 1.8 represent the distinct frequency components of the electrical (and optical) field(s) incident on the material. By examining different combinations of such field frequencies, one can identify the four consequences of the second-order nonlinear susceptibility: sum frequency generation (SFG), difference frequency generation (DFG), second harmonic generation (SHG), and optical rectification (OR).

When two optical fields with frequencies ω_1 and ω_2 are incident on a sample such that $\omega_3=\omega_1+\omega_2$, the summation over ω_n and ω_m in Equation 1.8 can be performed to yield

$$P_i\left(\omega_3\right)=\epsilon_0\sum_{jk}\left[\chi^{(2)}_{ijk}\left(\omega_3,\omega_1,\omega_2\right)E_j\left(\omega_1\right)E_k\left(\omega_2\right)+\chi^{(2)}_{ijk}\left(\omega_3,\omega_2,\omega_1\right)E_j\left(\omega_2\right)E_k\left(\omega_1\right)\right]. \tag{1.9}$$

Since j and k are dummy variables, they can be exchanged in the second term. Furthermore, for convenience we can introduce the intrinsic permutation symmetry of the nonlinear susceptibility which states that the nonlinear susceptibility is unchanged under si-

multaneous exchange of the last two frequency arguments and last two Cartesian indices. In short:

$$\chi^{(2)}_{ijk}\left(\omega_n+\omega_m,\omega_n,\omega_m\right)=\chi^{(2)}_{ikj}\left(\omega_n+\omega_m,\omega_m,\omega_n\right). \tag{1.10}$$

Physically, this condition states that it does not matter which field is first or second in the product of $E_j\left(\omega_n\right)E_k\left(\omega_m\right)$. Thus, Equation 1.9 can be succinctly written as

$$P_i\left(\omega_3\right)=2\epsilon_0\sum_{jk}\left[\chi^{(2)}_{ijk}\left(\omega_3,\omega_1,\omega_2\right)E_j\left(\omega_1\right)E_k\left(\omega_2\right)\right]. \tag{1.11}$$

In fact, in general, performing the summation over the field frequencies in Equation 1.8 yields

$$P_i\left(\omega_n+\omega_m\right)=\epsilon_0 D\sum_{jk}\left[\chi^{(2)}_{ijk}\left(\omega_n+\omega_m,\omega_n,\omega_m\right)E_j\left(\omega_n\right)E_k\left(\omega_m\right)\right], \tag{1.12}$$

where D describes the number of distinct permutations of ω_n and ω_m.

The specific process described by Equation 1.11, whereby two input fields of different frequencies cause a polarization output with frequency $\omega_3=\omega_1+\omega_2$ is known as sum frequency generation. However, when these two input fields interact, they also produce an output that oscillates with frequency $\omega_3=\omega_1-\omega_2$. This process is known as difference frequency generation and occurs because the definition of each field as in Equation 1.4 includes the presence of the complex conjugate which introduces a $e^{+i\omega_n t}$ term. Mathematically, DFG resembles the SFG described by Equation 1.11 when $\omega_2\rightarrow-\omega_2$.

Each frequency component of the incident field also interacts with itself and it's complex conjugate. These processes are known as second harmonic generation and optical rectification, respectively.

Optical rectification, or OR, again mathematically resembles the SFG described by Equation 1.11 when $\omega_2\rightarrow-\omega_1$ such that the output polarization has $\omega_3=0$. There are still two different frequencies (ω_1 and $-\omega_1$) interacting, so the number of permutations accounted for by D in Equation 1.12 is still equal to two. However, it is important

to note that optical rectification is the result of an incident field interacting with itself rather than two separate fields with the same frequency interacting with each other. The difference can be seen, for example, in pump-probe experiments where both time delay-independent optical rectification and time delay-dependent difference frequency generation are present.

Second harmonic generation is also the result of an incident field interacting with itself, leading to an output with double the incident frequency. When second harmonic generation occurs, the polarization is given by

$$P_i\left(2\omega_1\right) = \epsilon_0 \sum_{jk} \left[\chi^{(2)}_{ijk}\left(2\omega_1, \omega_1, \omega_1\right) E_j\left(\omega_1\right) E_k\left(\omega_1\right)\right], \tag{1.13}$$

rather than by Equation 1.11 because the sum over ω_n and ω_m in Equation 1.8 only yields one term. In other words, there is only one possible permutation of the input frequencies. This creation of a field with twice the input frequency is known as second harmonic generation and is commonly used to calculate the second-order nonlinear susceptibility at a given frequency.

In a pump-probe experiment, like the one performed by Schumacher et al. where both the pump and the probe have the same frequency, all four of these nonlinear optical processes are present. First, there is second harmonic generation stemming from interactions of the pulses with themselves. Then, there is optical rectification stemming from the interactions of the pulse electric fields with their own complex conjugates, which have negative frequencies. Finally, there is sum and difference frequency generation due to the interactions between the time-delayed pulses (and their complex conjugates) [10,11].

1.3 Atomic Force Microscopy

An atomic force microscope, or AFM, is a powerful, surface-sensitive tool for nanoscale characterization of atomic structures which traces contours of constant forces and is even

capable of resolving single molecules [12]. The first AFMs functioned as a tip which was scanned over the surface of a sample. This tip was mounted on a cantilever, whose deflection was measured in order to track the forces acting between the tip and the sample and thus, the topography of the surface [13].

This technique, known as static mode AFM, was soon supplemented by dynamic methods in which the tip scanning over the surface is excited at or near its resonance frequency. This can be achieved for example by using a piezoelectric actuator, an oscillating magnetic field, or even an optical excitation scheme. Forces between the tip and sample then result in a measurable change in the oscillation of the cantilever. Because these dynamic modes are sensitive to the net force acting between the tip and the sample, they can be used to measure a wide variety of tip-sample interactions including long-range attractive forces such as van der Waals interactions, electrostatic forces, or chemical forces and short-range repulsive forces such as Pauli-exclusion interactions or Coulomb interactions [14].

When it comes to dynamic AFM, two main operating modes have emerged: amplitude modulation (AM-AFM) and frequency modulation (FM-AFM). As their names indicate, these modes differ in the oscillation parameter used to extract sample properties.

1.3.1 Amplitude Modulation

In AM-AFM, also known as tapping mode, feedback electronics are used to change the tip-sample separation and hold the cantilever's oscillation amplitude constant. In this scheme, the cantilever is driven at a constant frequency, either at or near its natural resonance frequency.

Generally, the cantilever's motion can be approximated as a damped-driven harmonic oscillator whose equation of motion is given by,

$$m\ddot{z} + kz + \frac{m\omega_0}{Q}\dot{z} = F_{ts} + F_0\cos(\omega t), \tag{1.14}$$

where z is the cantilever's motion, and m, k, ω_0, and Q are the mass, force constant, angular resonance frequency, and quality factor of the free cantilever. F_0 and ω are the amplitude and angular frequency of the applied driving force and F_{ts} describes the tip-sample interaction force [15]. This harmonic approximation allows the cantilever motion, z, to be written as,

$$z = A\cos(\omega t - \phi) + Be^{-\alpha t}\cos(\omega_r t + \beta), \tag{1.15}$$

where ω_r is the damped resonance frequency of the cantilever and the second term describes the transient motion of the cantilever decaying with a time constant $\alpha = \omega_0/2Q$. The first term then represents the steady state solution wherein the cantilever oscillates sinusoidally with an amplitude A. In the absence of tip-sample interactions, the amplitude of the steady state solution can be approximated as a Lorentzian function shown in Figure 1.2 where,

$$A(\omega) = \frac{F_0/m}{\sqrt{(\omega_0^2 - \omega^2)^2 + (\omega\omega_0/Q)^2}}. \tag{1.16}$$

The phase of the cantilever oscillation in this case is also shown in Figure 1.2 and described by,

$$\tan\phi = \frac{\omega\omega_0/Q}{\omega_0^2 - \omega^2}. \tag{1.17}$$

Thus, when the cantilever is driven at its natural resonance frequency ($\omega = \omega_0$), the amplitude is,

$$A(\omega = \omega_0) = \frac{QF_0}{k}, \tag{1.18}$$

where k is the force constant, $k = m\omega^2$ [14].

When the tip-sample force gradient, $\frac{dF_{ts}}{dz}$, is approximately constant over the oscillation amplitude, A, the effective force constant can be written relative to the 'free' force constant as,

$$k_{eff} = k - \frac{dF_{ts}}{dz} \tag{1.19}$$

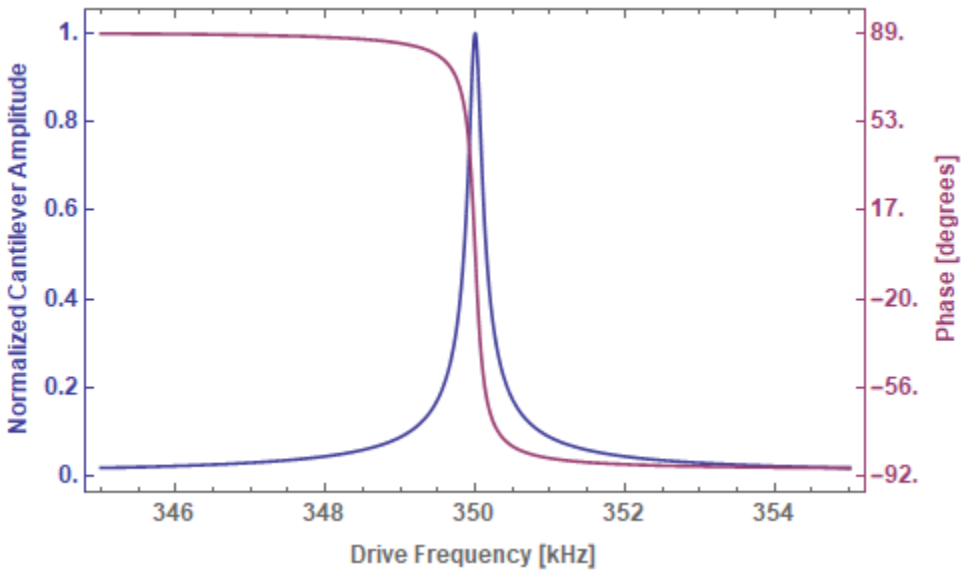

Figure 1.2: Model of amplitude and phase of a cantilever with a Q factor of 2,000 and a resonance frequency of 350kHz. The amplitude is given by Equation 1.18, and the phase is given by Equation 1.17.

which in turn results in a modified resonance frequency of,

$$\omega_{eff} = \sqrt{\frac{k - \frac{dF_{ts}}{dz}}{m}}. \tag{1.20}$$

In this approximation, the new resonance frequency then corresponds to a shift of the curves in Figure 1.2 along the frequency axis where ω_0 is replaced by ω_{eff}. As the curves shift, the amplitude of the cantilever oscillations at a given drive frequency is also changed. When the force gradient, $\frac{dF_{ts}}{dz}$, is small, the amplitude change can be approximated as,

$$\Delta A = \frac{2A_0 Q}{3\sqrt{3}k}\frac{dF_{ts}}{dz}. \tag{1.21}$$

Thus, by tracking the amplitude of the cantilever's oscillation at a given frequency, it is possible to spatially resolve changes in tip-sample interactions [14]. Practically, amplitude modulated AFM changes the tip-sample separation in order to maintain a constant can-

tilever oscillation amplitude using feedback electronics. This scheme is also often referred to as slope detection.

It should be noted that while this approximation provides a good insight into the behavior of the cantilever [15], it is often not valid in tapping mode because of nonlinearities in the tip-sample interaction forces. Specifically, the force gradient is not constant with z and, therefore, becomes amplitude dependent. Thus, in true tapping mode, where both F_{ts} and $\frac{dF_{ts}}{dz}$ are large, the solution to Equation 1.14 becomes nonlinear.

In general, from Equation 1.21, a cantilever with a higher quality factor, Q, will have a larger change in amplitude for a given tip-sample interaction, making it more sensitive to small forces. Higher Q factors are achieved, for example, through operation in vacuum conditions, which is also practical for applications in which clean surfaces are necessary.

However, it is important to also consider the cantilever's transient motion described in Equation 1.15, which decays with a time constant proportional to Q. Thus, higher Q factors require more time to reach the steady state condition required for tracking their amplitude. Therefore, while higher Q factors lead to increased sensitivity in AM-AFM, they also lead to longer required measurement times. This is one of the major drawbacks of amplitude-modulated AFM.

1.3.2 Frequency Modulation

In light of the fundamental limitations of amplitude modulated AFM (such as the need to operate at low Q factors), a frequency modulated scheme was developed. This method of atomic force microscopy is well-suited to operation in vacuum with high Q factor cantilevers.

In contrast to AM-AFM, which tracks the amplitude of a cantilever at a given frequency, FM-AFM tracks the resonance frequency of the cantilever directly as shown in Figure 1.3.

The cantilever is oscillated continuously at its instantaneous resonance frequency using an oscillation control amplifier that takes the displacement of the cantilever, phase

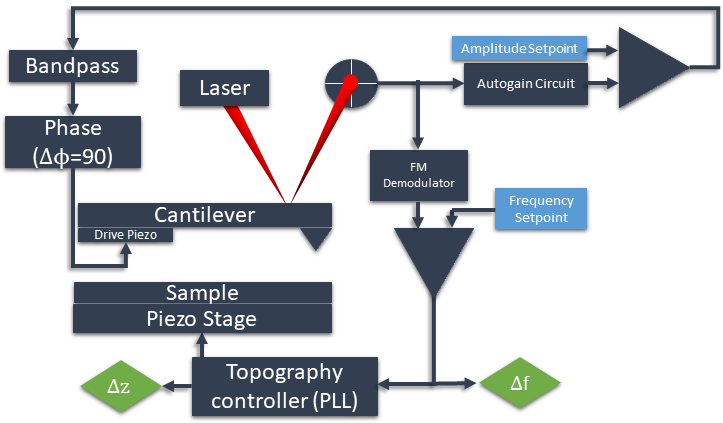

Figure 1.3: Diagram of typical FM-AFM setup. The cantilever's position is tracked using a laser beam and photodetector. The position is then fed into an amplitude controller where a gain and a 90 degree phase shift are applied to keep a constant amplitude. It is also input into a frequency demodulator where a phase-locked loop (PLL) is used to determine the piezo stage position and maintain a constant tip-sample separation. The output signals of frequency shift (Δf) and piezo position (Δz) are recorded.

shifts it by 90 degrees, and applies a gain to keep the amplitude constant. This direct, self-oscillation scheme means that the system can respond to changes in the resonant frequency within a single oscillation and is no longer limited by the Q factor of the cantilever [14, 15].

The current resonant frequency of the cantilever can then be directly measured from its deflection using a phase-locked loop (PLL). A feedback circuit is then used to change the tip-sample distance and maintain a constant frequency shift.

Analytically, the motion of the cantilever in this scheme can still be approximated as a damped-driven harmonic oscillator. Thus, when $k_{ts} << k$, the cantilever's frequency shift can be approximated as in Equation 1.20 and written as,

$$\Delta\omega = \frac{\omega_0 k_{ts}}{2k}, \tag{1.22}$$

such that the frequency shift is proportional to the force gradient [15]. The harmonic approximation holds when the force gradient is constant over the oscillation amplitude

of the cantilever. This is typically true for electrostatic and magnetic forces, where the force gradient is small compared to the amplitude, or for small oscillation amplitudes.

When the oscillation amplitude of the cantilever is large compared to the tip-sample interaction range, this linear approximation is no longer valid and the frequency shift must be calculated through a perturbation scheme. While many such schemes have been used, Garcia et al. note that they share a common relation between tip-sample forces, F_{ts}, and frequency shift, $\Delta\omega$,

$$\Delta\omega(d, k, A_0, \omega_0) = -\frac{\omega_0}{kA_0^2}\langle F_{ts} z\rangle = -\frac{1}{2\pi}\frac{\omega_0}{kA_0}\int_0^{2\pi} F_{ts}[d + A_0 + A_0\cos\phi]\cos\phi d\phi, \qquad (1.23)$$

where $\langle F_{ts}\rangle$ is the average tip-sample interaction force averaged over an oscillation cycle and d is the distance of closest approach [15].

Thus, the frequency shift measured in FM-AFM is directly related to the average tip-sample interaction force, allowing for spatial resolution of topography, electrostatics, or other interacting forces.

1.4 Measuring Nonlinear Optical Effects with AFM

Traditionally in optics, a material's response to excitation by light is measured as light reflected, transmitted, absorbed, or emitted from the material. This means that the nonlinear optical response, for example, is typically characterized by looking at sum frequency and second harmonic generation. As discussed in Section 1.2, these effects are caused by oscillating polarization induced in the material which lead to the emission of light at the oscillation frequency. However, in addition to these oscillating terms, nonlinear optical interactions in a material also result in zero-frequency terms known as difference frequency generation and optical rectification. In other words, when light interacts nonlinearly within a material, a constant polarization is induced.

Section 1.3 describes how atomic force microscopes respond to all forces acting between the tip and the sample. Notably, this includes electrostatic forces, such as those arising from a polarization or electric field inside the material.

The impact of electrostatic forces can be derived by considering tip-sample interaction forces, F_{ts} as the gradient of the potential between the tip and the sample, U_{ts}. Then, one can write

$$F_{ts} = -\frac{\partial U_{ts}}{\partial z_{ts}}. \tag{1.24}$$

For electrostatic interactions, this tip-sample potential is related to the charge density in the tip and the sample (ρ_t and ρ_s) as well as the electrostatic potentials of both (V_t and V_s) by,

$$U_{ts} = \frac{1}{2}(\int_t \rho_t(z)V_t(z)dz + \int_s \rho_s(z)V_s(z)dz), \tag{1.25}$$

where the first term is integrated over the tip and the second term is integrated over the sample along the z axis.

In metals or semiconductors with minimal band bending, it is generally reasonable to assume that the tip and sample voltages and charge densities are independent of z. Then, Equation 1.25 can be simplified to

$$U_{ts} = \frac{1}{2}Q_{ts}V_{ts} = \frac{1}{2}C_{ts}V_{ts}^2, \tag{1.26}$$

where $Q_{ts} = \int_s \rho_s dz = -\int_t \rho_t dz$, $V_{ts} = V_t - V_s$, and C_{ts} is the capacitance between the tip and the sample.

Substituting Equation 1.26 into Equation 1.24 in turn yields an electrostatic tip-sample interaction force of,

$$F_{electrostatic} = \frac{1}{2}\frac{\delta C_{ts}}{\delta z}V_{ts}^2, \tag{1.27}$$

for metal tips interacting with samples that are metal or have negligible band banding [16].

The tip-sample potential V_{ts} describes any and all electrostatic potentials between the tip and the sample. This includes, for example, the work function difference, $\frac{\Delta\phi}{e}$, also known as the contact potential difference. In addition, it is often interesting to experimentally apply a bias to the sample using a back electrode. This bias may be constant or modulated, depending on the experiment being performed, such as electrostatic force microscopy (EFM) or Kelvin probe force microscopy (KPFM).

As discussed in Section 1.2, when a strong electric field is incident on a nonlinear optical material, a polarization is induced within that material. This nonlinear optical polarization, in turn, yields an electrostatic potential within the material such that,

$$V_s(\vec{r}) = \frac{1}{4\pi\epsilon_0}\left(\int_S \frac{\vec{P_{NLO}}\cdot\hat{n}}{r}da' + \int_V \frac{-\vec{\nabla}\cdot\vec{P_{NLO}}}{r}d\tau'\right), \tag{1.28}$$

where the first term describes the potential due to the bound charges at the surface while the second term describes the potential due to the charge density within the material. When it comes to second order nonlinearities, the polarization, and therefore the potential, has both DC and oscillating components caused by OR, DFG, SHG, and SFG as discussed in Section 1.2. Thus, the nonlinear optical response of a material induces an electrostatic potential between the tip and the sample, which directly contributes to the tip-sample interaction forces as described by Equations 1.27 and 1.28.

Importantly, Equation 1.23 shows that the frequency shift detected in an FM-AFM is proportional not to the force, but rather to the average of the force over an oscillation cycle, $\langle F_{ts}\rangle$. Therefore, when the resonance frequency of the cantilever, ω_r, is much lower than the frequency of an oscillating potential, f_{mod}, the potential will be averaged out over the course of the cantilever's oscillation. In this experiment, cantilevers with a resonant frequency of 350 kHz are used, while the polarization induced from light-matter interactions has components oscillating at zero, one and two times the frequency of the incident light, $\approx 4\times10^{14}$ Hz and $\approx 8\times10^{14}$ Hz respectively. Thus, only the zero-frequency opti-

cal rectification and difference frequency generation components of the nonlinear optical response contribute to the AFM response.

1.5 Optical Excitation

In order to observe the non-linear optical polarization in a material, it is first necessary to optical excite the material. In this experiment, the optical excitation is achieved using a pulsed laser as described in Section 2.1. Specifically, the magnitude of the nonlinear response is probed by performing an optical autocorrelation measurement.

1.5.1 Autocorrelation

Optical autocorrelations are typically used as a standard method of characterizing the shape and length of a short laser pulse. In an ideal world, such a characterization would be performed by using a reference pulse with a known form. When the reference signal is shorter than the signal of interest, the whole temporal shape of the unknown signal can be found by varying the relative time delay between the two pulses [17]. Mathematically, this is equivalent to convolving the known signal with the unknown, such that,

$$A_{\text{conv}}(\tau) = I_s \circledast I_{\text{ref}} = \int_{-\infty}^{+\infty} I_s(t) I_{\text{ref}}(t-\tau) dt, \tag{1.29}$$

where A_{conv} is the convolution, also known as the cross-correlation, of the signal and the reference as a function of the temporal delay τ between them [17]. If the reference signal is infinitely short in comparison to the signal or interest, the function I_{ref} can be approximated as a Dirac delta function and the temporal profile of the unknown signal of interest can be exactly described as a function of τ.

Unfortunately, it is impossible to produce an infinitely short reference pulse, especially in comparison to an ultra-fast femtosecond pulse like those used in this experiment. When the reference and initial signals approach each other in duration, the convolution

signal becomes temporally smeared. Nonetheless, as long as the shape of the reference signal is known, the initial signal can still be extracted by deconvolution. Thus, in order to accurately characterize the initial pulse, the reference signal must be either well defined or considerable shorter than the signal of interest [17]. Practically, both of these conditions are difficult, if not impossible, to achieve for an ultra-fast laser pulse like the ones used in this experiment.

Instead, ultrafast light pulses are typically characterized via an autocorrelation, or auto-convolution, measurement. That is, pulses from the same source are combined with a variable time delay between them. This can be achieved using an interferometric setup, wherein the pulsed laser beam is split using a beamsplitter and one half of the beam is delayed with respect to the other before they are recombined. By sweeping this delay, an autocorrelation measurement can then be taken using a traditional detector such as a photodetector or CCD camera.

In the simplest setup, the resulting measurement is the linear field-autocorrelation, which describes the addition of two identical, time-delayed pulses integrated over time by a photodetector and is given by,

$$A_{FAC} = \int_{-\infty}^{+\infty} |E(t) + E(t-\tau)|^2 dt = 2\int_{-\infty}^{+\infty} |E(t)|^2 dt + 2\mathrm{Re}[\int_{-\infty}^{+\infty} E(t)E*(t-\tau)dt], \quad (1.30)$$

where E(t) is the electric field of the pulses and E*(t) is its complex conjugate. The first term of this field-autocorrelation is constant with respect to the time delay τ and describes the integrated intensity of the individual arms of the interferometer with no interference effects, while the second term oscillates in τ and is known as the pulse first order correlation function [17]. This second term is particularly interesting, as its Fourier transform is equivalent to the spectral intensity distribution of the pulse, $S(\omega) = |\tilde{E}(\omega)|^2$, where $\tilde{E}(\omega)$ is the Fourier transform of $E(t)$ [18]. For a Gaussian pulse, the resulting field-autocorrelation is shown on the left in Figure 1.4.

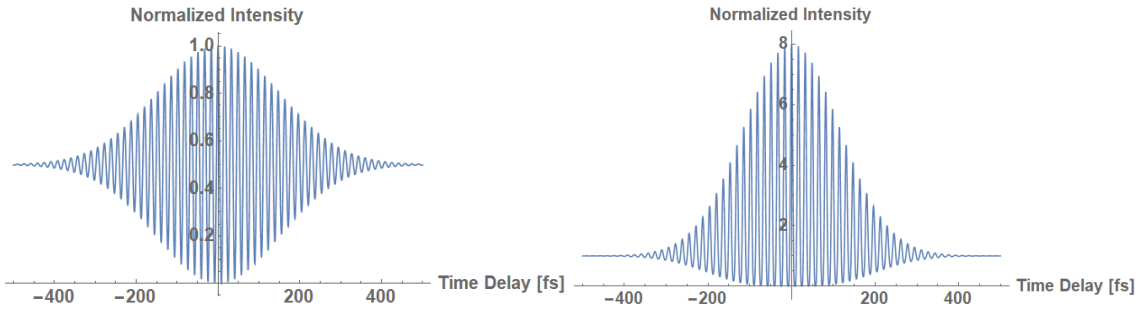

Figure 1.4: Linear field-autocorrelation function (left) and second order interferometric autocorrelation (right) of a 780nm Gaussian pulse with a full width half maximum of 150fs. Both autocorrelation functions are normalized with a field amplitude of 1.

The only temporal information that can be extracted from this linear field autocorrelation is the pulse coherence time, which is the reciprocal of the spectral width of the pulse. This is not the same as the pulse length, but rather a measure of how monochromatic the laser pulses are. Therefore more information is required to fully characterize the temporal shape of these ultrafast pulses.

One very effective method of extracting this information is by measuring the second-order autocorrelation of the pulse. Experimentally, this is achieved by focusing the output of an interferometer, like the one used to measure the field-autocorrelation, onto a crystal that exhibits a strong non-linear optical response as described in Section 1.2. In this case, a BBO crystal is used.

The total signal emitted from the crystal is related to the polarization within the material and described by

$$A(\tau) = \int_{-\infty}^{+\infty} |P(t,\tau)|^2 dt, \tag{1.31}$$

where $A(\tau)$ is the amplitude of the emitted field and the polarization $P(t,\tau)$ is expanded into higher order terms as described in Equation 1.1 such that [18,19],

$$P(t,\tau) = \epsilon_0 \chi^{(1)}(E(t) + E(t-\tau)) + \epsilon_0 \chi^{(2)}(E(t) + E(t-\tau))^2 + ... \tag{1.32}$$

Thus, the full amplitude of the emitted field is given by,

$$A(\tau) = \int_{-\infty}^{+\infty} |\epsilon_0 \chi^{(1)}(E(t) + E(t-\tau))|^2 dt + \int_{-\infty}^{+\infty} |\epsilon_0 \chi^{(2)}(E(t) + E(t-\tau))^2|^2 dt + ... \quad (1.33)$$

The first term of this autocorrelation is identical to the field autocorrelation described by Equation 1.30 oscillates in time with a frequency of 1ω, while the second term describes the so-called fringe-resolved intensity autocorrelation (FRIAC), also known as the interferometric autocorrelation. This interferometric autocorrelation includes terms that oscillate in time with 0ω and 2ω as described in Section 1.2. Typically, the first, linear term in Equation 1.31 is filtered out experimentally using a bandpass filter such that only the second-order autocorrelation is measured [18].

Expanding the second term of Equation 1.31 yields a more specific form of this interferometric autocorrelation, such that,

$$\begin{aligned} A^{(2)}_{FRIAC}(\tau) = \int_{-\infty}^{+\infty} I^2(t) + I^2(t-\tau) dt \\ + 4 \int_{-\infty}^{+\infty} I(t) I(t-\tau) dt \\ + 2 \int_{-\infty}^{+\infty} (I(t) + I(t-\tau)) E(t) E^*(t-\tau) dt + c.c. \\ + 2 \int_{-\infty}^{+\infty} E^2(t) E^{*2}(t-\tau) dt + c.c., \end{aligned} \quad (1.34)$$

where $I(t) = |E(t)|^2$ [17, 18]. The first term in Equation 1.34 is independent of τ and corresponds to the second harmonic generation caused by the individual pulses interfering with themselves within the crystal. The autocorrelation is often normalized with respect to this term, leading to a normalized amplitude of 8. The second term describes the envelope shape of the autocorrelation, which varies as a function of τ but has no oscillatory component. In contrast, the third and fourth terms both oscillate in time delay τ with frequencies ω and 2ω respectively. These oscillations result from the interference between the two pulses within the NLO crystal and account for the fringes in the *fringe resolved*

intensity autocorrelation. The shape of this normalized intensity autocorrelation for two Gaussian pulses is shown on the right in Figure 1.4.

Information about the temporal shape and duration of the pulse is extracted by assuming a pulse shape, usually Gaussian, and performing a deconvolution of the autocorrelation trace [17].

In this experiment, the autocorrelation is used not only to characterize the pulses outside of the vacuum, but also to measure the nonlinear optical response of the sample, since the amplitude of the autocorrelation can be directly related to the susceptibility $\chi^{(2)}$ as shown in Equation 1.31. To achieve this, the output of the interferometer is split into two paths: one is directed to a photodetector which measures the optical autocorrelation described above, while the other is directed into the UHV-AFM and onto the sample surface as shown in Figure 1.5. Thus, the light entering the AFM consists of two time-delayed pulses as described by Equation 1.30 and shown in Figure 1.4, which interact in the sample to produce a polarization as described in Section 1.2. This polarization, in turn, causes a detectable frequency shift as described in Section 1.4. It is important to note that autocorrelation measurements are typically described in terms of the optical intensity of the emitted light, given by $I(t) = \int_{-\infty}^{+\infty} |P(t)|^2 dt$, where the induced polarization is integrated by the photodetector used for measuring. In AFM, in contrast, the polarization manifests as a tip-sample interaction force which is measured by the frequency shift of the cantilever as described by Equation 1.23. Thus, in the AFM integration of the autocorrelation signal over time is performed by the cantilever rather than by a photodetector.

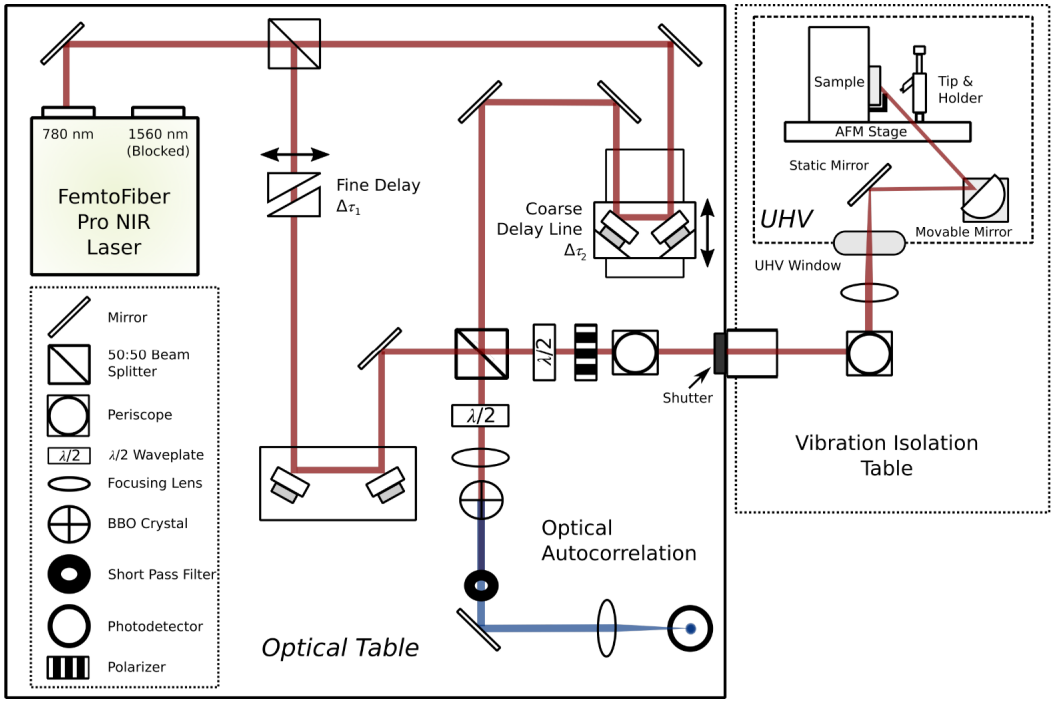

Figure 1.5: Interferometric optical setup used for this experiment. A 780nm beam output from the Femtofiber Pro NIR laser is directed into two arms by a 50/50 beamsplitter. The first arm is delayed using a fine, wedge delay while the second arm is delayed using a free-space optical delay line. In this work, only the free-space delay was utilized. The beams are then recombined using another 50/50 beamsplitter. Half of this recombined beam is focused on a BBO crystal and then a photodetector to measure the interferometric autocorrelation. The other half is directed into the AFM using a series of periscopes and a slip-stick piezo-controlled movable mirror. Figure adapted from [20].

Chapter 2

Methods Characterization

2.1 Hardware

2.1.1 Ultra High Vacuum AFM

The bulk of this work was performed using a commercial JEOL JSPM 4500A UHV AFM as shown in Figure 2.1. This system consists of three main chambers: one for transfers in an out of vacuum, one for sample preparation and one for measurements. The sample preparation chamber features capabilities for molecule evaporation, metal evaporation, ion sputtering, crystal cleaving, low-energy electron diffraction measurements (LEED), and Auger electron spectroscopy (AES). Samples and cantilevers can be transported from the transfer chamber to a carousel within the preparation chamber using a magnetically-coupled transfer arm. The sample or cantilever is then moved to the main measurement chamber via another transfer arm. In addition to the AFM, the measurement chamber also contains a scanning electron microscope (SEM) for further sample characterization.

The entire system is kept at ultra high vacuum in order to maintain clean sample surfaces and to improve the sensitivity of the AFM itself. The sample preparation chamber's base pressure is 4×10^{-11}mbar while the measurement chamber has a base pressure of

4×10^{-10}mbar. The measurement chamber has a slightly lower base pressure due to a small leak from an o-ring seal of the attached SEM.

The vacuum in the system is achieved and upheld through a series of pumps. Firstly, a sliding vane rotary vacuum pump (Adixen 20120SD), which pumps 9.7 m^2/hr and can achieve a pressure on the order of 10^{-3} mbar, is used to back a turbo-molecular pump (Pfeifer TMU 261) which, for nitrogen, pumps about 210 L/s. This turbo pump can achieve pressures down to about 10^{-6}mbar. Additionally, both the preparation and measurement chambers are equipped with a diode type sputtering ion pump (Satsuki SIP-300XH-T16) and a titanium sublimation pump (ULVAC PGT-3F) which allow the system to routinely reach base pressures on the order of 10^{-11} in the preparation chamber and 10^{-10} in the main chamber.

The AFM sample stage features a piezo-driven stage for fine positioning along with a mechanical coarse positioning system controlled by external motors coupled to the sample stage through rotary feedthroughs. The coarse motors enable positioning of the cantilever on the sample surface within a range of 2 mm in both the x and y positions. The fine positioning is controlled by a piezo tube which extends 5 μm in the x and y directions and 1.4 μm in the z direction.

In this system, the cantilever's position is probed using a beam deflection scheme. A laser diode (Hitachi HL6714G) with a wavelength of 670 nm is focused onto the cantilever, and the reflected light is directed onto a 4-quadrant photodiode which allows for localization of the beam and, therefore, a readout of the cantilever's position. The laser diode is operated using a low noise controller (Thorlabs LDC 201C) at constant current. In addition, there is a bandpass filter (Chroma Technology Corp, NC611498, ET679/30nm) placed in front of the photodiode to filter out stray light, either from the ambient environment or from the ultrafast laser used for optically-pumped experiments [20,21].

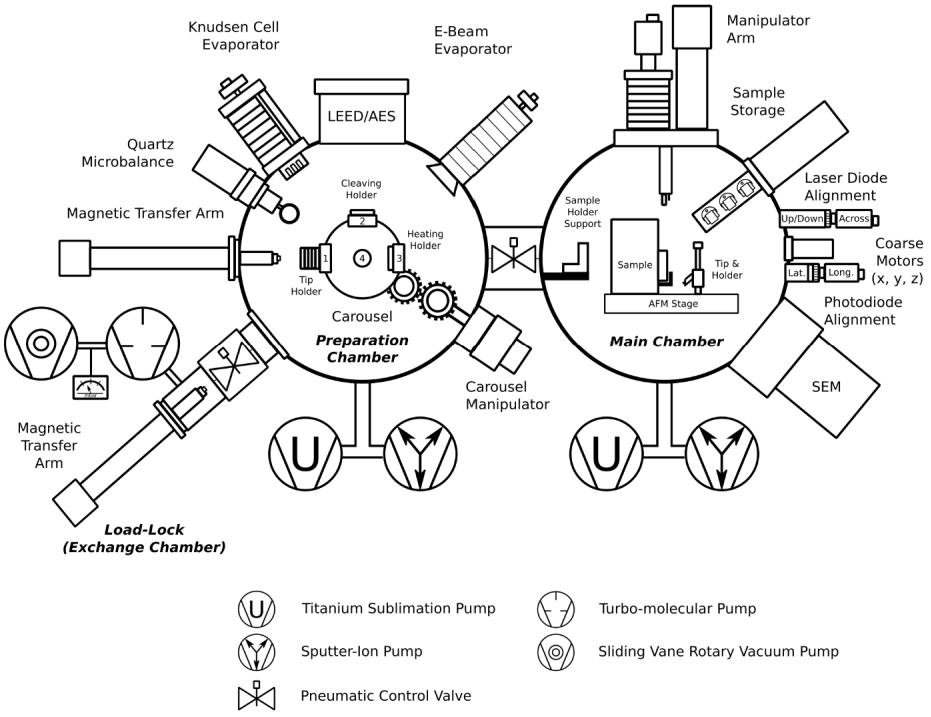

Figure 2.1: Diagram of JEOL JSPM 4500A UHV AFM including the transfer chamber, the sample preparation chamber, and the main measurement chamber. The sample preparation chamber includes a Knudsen cell evaporator, an electron beam evaporator, a quartz microbalance, a low energy electron diffraction microscope, and an Auger electron spectroscope, while the measurement chamber contains the AFM along with an attached SEM. Figure adapted from [20].

2.1.2 Optics Integration

The optical excitation used for this work is achieved by directing a high power laser beam into the UHV-AFM system. Specifically, a mode-locked, 100 femtosecond laser beam from a fiber-based Toptica FemtoFiber Pro near infrared (NIR) laser is used. This laser consists of an Er-doped core that is directly pumped by fiber-pigtailed laser diodes. A ring cavity with a saturable absorber mirror selects and amplifies pulses of a specific amplitude, leading to mode-locked operation of the laser. Ultimately, pulses produced by this system have a repetition rate of 80 MHz and a center wavelength of 1560 nm. The system also features a second beam with a wavelength of 780 nm which is produced by direct-

ing the fundamental beam toward a lithium niobate (PPLN) crystal to stimulate second harmonic generation. Because of the frequency doubling procedure, this 780nm output has a power of about 140 mW, decreased from the fundamental frequency power of 350 mW. The higher frequency beam is used exclusively in this experiment, as it lies near an exciton peak of WS2 and, therefore, is expected to produce a stronger non-linear optical response.

The emitted 780 nm pulsed laser beam is directed into an interferometer as shown in Figure 1.5, where one output is passed into the UHV-AFM. The light entering the UHV system is first incident on a static mirror and then on a movable mirror which directs the beam into the tip-sample junction. The movable mirror is based on slip-stick piezos and can be externally controlled [21].

Importantly, because the integration of the optics with the AFM is done without the use of optical fibers, the interferometric setup can be mounted on a separate optical table such that the mechanical vibrations from the optical and AFM systems are decoupled. In addition, the setup is located on a concrete slab foundation directly on bedrock, separated from the rest of the building, in order to further minimize vibrations.

2.2 Molecular Model System

Previously, this system has been used to measure autocorrelation functions (as described in Section 1.5) on both lithium niobate crystals and few-layer molybdenum disulfide samples [11, 20]. These measurements were done with the goal of achieving ultrafast time resolution in a pump-probe AFM setup. However, as discussed in Sections 1.5 and 1.4, the amplitude of this autocorrelation is directly related to the nonlinear susceptibility of the material, $\chi^{(2)}$. Thus, this technique can also be used to extract the magnitude of the nonlinearity of a material.

In order to more thoroughly understand the origin of the optically-induced AFM signal, it is useful to first investigate a material with known properties. In this work, the ef-

fect of $\chi^{(2)}$ on the AFM measurement was studied by looking at the behavior of molecules with a well-known, large dipole moment and correspondingly large $\chi^{(2)}$. Specifically, a spin-coated layer of the merocyanide dye HB238 was used. A 24nm thick layer of the dye, whose structure is shown in Figure 2.2, was spin-coated onto a glass substrate and then annealed at 150°C. This annealing process has been shown to cause the molecules to align "edge-on" [22], leading to a stronger nonlinear constant. These molecules, which are highly polar and π-conjugated, have recently been of interest in the world of organic photovoltaics, as they have been shown to have higher transport properties than expected due to their tendency to self-assemble into quasi-centrosymmetric dimers [23,24]. The individual molecules, however, are noncentrosymmetric and are expected to exhibit strong nonlinearities on the scales probed by an AFM [23].

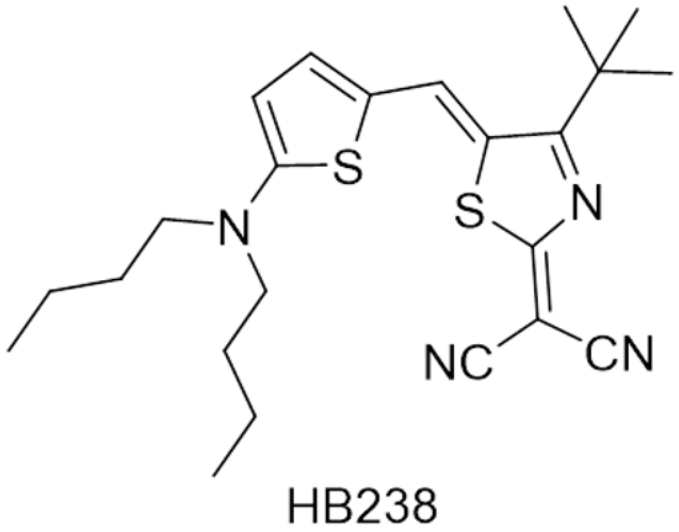

Figure 2.2: Diagram of the structure of an HB238 molecule, a type of merocyandide dye with a noncentrosymmetric structure and large dipole moment. When a thin-film of these molecules is annealed, the molecules have been shown to align into a structured, 'edge-on' formation [22]. Figure adapted from [23].

A topography measurement of the molecular thin-film taken using non-contact, frequency modulated AFM under UHV conditions is shown in Figure 2.3. There are a few

quasi-triangular crystals at the surface, which are believed to have grown on top of the molecules after the annealing process.

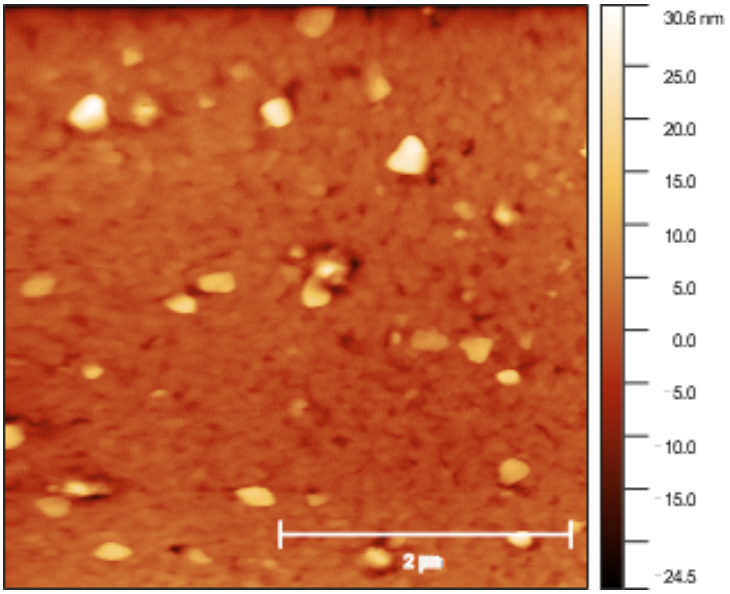

Figure 2.3: Topography image of a thin film of HB238. The quasi-triangular flakes are likely crystals that have grown over time on top of the molecules after tempering. This image was taken using fm-AFM in UHV with a frequency shift setpoint of -2Hz and a cantilever oscillation amplitude of 6nm.

Due to their high nonlinearity, these molecules were used to better understand the behavior of the AFM signal and noise as a function of power, delay position, and applied bias as discussed in Sections 2.3 and 2.4.

2.3 Autocorrelation Measurements

When measuring the optical and electrostatic properties of these molecules with our optically excited AFM, we have the opportunity to more fundamentally understand the measurement technique and the origin of the signal.

For example, it is vital to understand the interplay between linear and nonlinear optical effects within the material. One way to distinguish the two is by studying the system's dependence on the power of the incident light. Based on Equation 2.3, one might expect

that the first order polarization would scale linearly with power, while the second order polarization would scale quadratically. Of course, the AFM measures frequency shifts, not polarization, but the quadratic power dependence of nonlinear optical effects should be retained. This is because the tip-sample interaction force, F_{ts}, is directly proportional to the square of the induced polarization, as can be seen from Equations 1.28 and 1.27. Then, Equation 1.2 tells us that the second-order polarization is proportional to the square of the electric field, so,

$$F_{nonlinear} \propto (P_{NLO})^2 \propto (|E_0|^2)^2. \tag{2.1}$$

Since the power of the incident light is defined by Power $= |E_0|^2$, one can easily see from Equation 2.1 that the tip-sample interaction forces caused by a nonlinear polarization are quadratically dependent on the power of the optical excitation, $F_{ts} \propto (\text{Power})^2$. In contrast, Equation 1.2 shows that a linear polarization is proportional only to E_0, such that the tip-sample interaction forces induced by a linear polarization depend only linearly on the power, $F_{linear} \propto (P_{linear})^2 \propto |E_0|^2 \propto$ Power.

Experimentally, the autocorrelation amplitude was found to increase quadratically as the incident laser power was tuned from 0 to about 70mW as shown in Figure 2.4. This was achieved by placing a half waveplate followed by a polarizer into the beam path. As the waveplate is rotated relative to the polarizer, the intensity of the resultant beam is tuned from 0 to about 70mW while the incident polarization is kept constant. The amplitude of the resulting autocorrelation measurement is extracted by fitting the envelope of the second-order autocorrelation as described by Equation 1.34 with two Gaussian pulses. A linear background is also added to account for slow drifts. The measured quadratic power dependence indicates the clear presence of a nonlinear polarization induced by the pulsed laser excitation.

The quadratic power dependence of the nonlinear polarization is something that is also observed in optical measurements of nonlinear effects like as second harmonic generation [25]. However, it is important to note that this mechanical AFM measurement of nonlinear optics is very different from these optical characterization methods. Thus, care

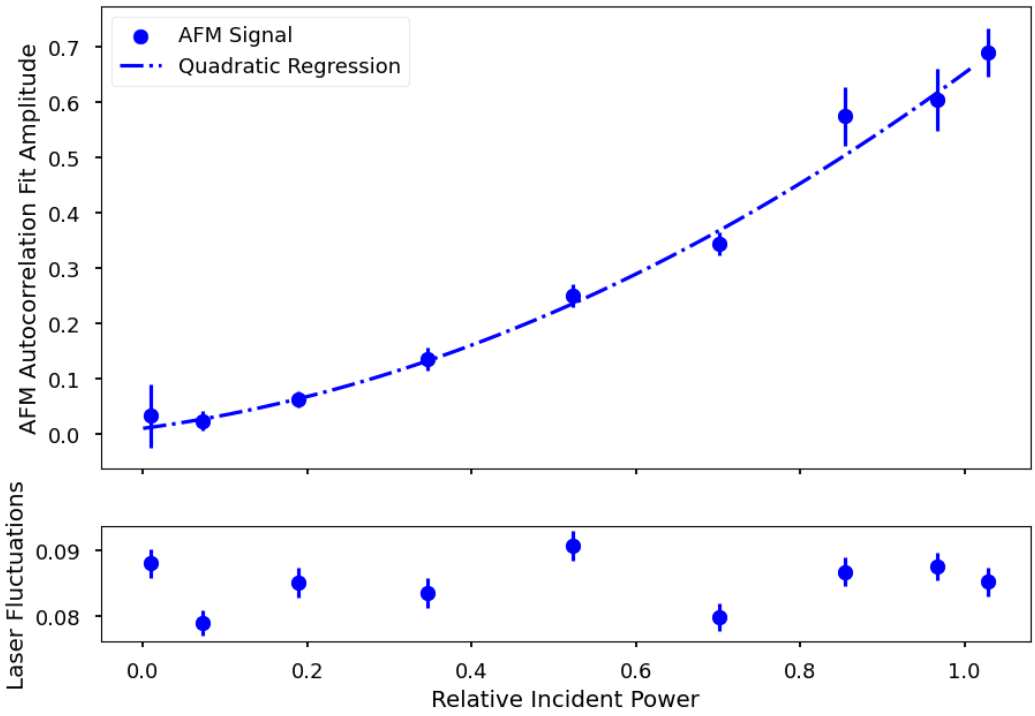

Figure 2.4: Amplitude of autocorrelation function measured on a thin film of HB238 with the AFM as a function of the power of the light incident of the sample surface. The amplitude increases quadratically with power as expected. The optical autocorrelation was also measured simultaneously to check for fluctuations in the laser power. The power was tuned while maintaining constant polarization by rotating a quarter waveplate relative to a polarizer. Each AFM autocorrelation was taken with a setpoint of -10Hz and a peak-to-peak cantilever oscillation amplitude of 6nm. The cantilever Q factor was 21,780. Additionally, the z-feedback was run with a low gain of 40 pm/Hz and a long time constant of 50ms to correct for slow drifts in the system.

must be taken to understand the origin of the signal and, importantly, the influence of the measurement technique.

One such influence is the presence of the tip close to the sample. In order to understand the consequences of bringing the tip close to the sample when measuring an optical effect, it is useful to consider a one-dimensional description of the nonlinear optically induced polarization.

In the simplest picture, one can approximate incoming light as a continuous wave described by,

$$E(t) = E_0 \cos(kz - \omega t), \tag{2.2}$$

where ω is its frequency. In this case, the polarization described by Equation 1.1 becomes,

$$P(t) = \frac{1}{2}\epsilon_0 \chi^{(2)} E_0^2 + \epsilon_0 \chi^{(1)} E_o \cos(kz - \omega t) + \frac{1}{2} E_0^2 \cos(2kz - 2\omega t) + ..., \tag{2.3}$$

where the polarization contains components oscillating at the frequency of the incident light, ω, as well as at $2 \times \omega$ and zero frequency. The AFM is sensitive to this zero-frequency component as described in Section 1.4.

Equation 2.3 now describes the polarization induced by a continuous wave optical excitation. However, it is important to note that in an AFM there is almost always an additional electrostatic field caused by the difference in work function between the tip and the sample, or the contact potential difference. In addition, it is common to directly apply an electric field between the tip and the sample to investigate electrostatic effects using techniques such as electrostatic force microscopy (EFM) or Kelvin force probe microscopy (KPFM). These tip-sample fields can have a significant magnitude, since they are applied over a very small distance, on the order of nanometers.

Thus, one must account for a zero-frequency component to the applied electric field in addition to the oscillating optical illumination, such that,

$$E(t) = E_{DC} + E_0 \cos(kz - \omega t). \tag{2.4}$$

Then, modifying Equation 2.3 to include this additional DC electric field yields,

$$\begin{aligned} P(t) = \epsilon_0 \chi^{(1)} E_{DC} + \epsilon_0 \chi^{(2)} [E_{DC}^2 + \frac{1}{2} E_0^2] \\ + \epsilon_0 [\chi^{(1)} + 2 E_{DC} \chi^{(2)}] E_0 \cos(kz - \omega t) \\ + \epsilon_0 \chi^{(2)} \frac{1}{2} E_0^2 \cos(2kz - 2\omega t) + ... \end{aligned} \tag{2.5}$$

Now, the $1 \times \omega$ and $0 \times \omega$ terms in the polarization described by Equation 2.5 depend on the DC electric field. The influence of this zero-frequency field on the $1 \times \omega$ term is often referred to as the Pockels effect and corresponds to a change in the refractive index of the material, $n = \sqrt{1 + \chi_{effective}}$, where $\chi_{effective} = \chi^{(1)} + 2E_{DC}\chi^{(2)}$.

For the AFM, it is particularly relevant to consider the change to the zero-frequency component, which now depends not only on E_0^2, but also on both E_{DC} and E_{DC}^2. Notably, the polarization related to E_{DC}^2 is also proportional to $\chi^{(2)}$ and one could imagine using an applied DC field to extract that magnitude of $\chi^{(2)}$ in place of optical excitation. In reality, this 'DC' electric field does not need to be constant. Instead, it could be modulated at a low frequency that is within the bandwidth of the phase-locked loop. This represents an exciting future path for this work which will be discussed in more depth in Section 4.2.

In addition to the signal resulting from the presence of the tip, one might also expect to observe light-induced effects in the material apart from the nonlinear polarization. For example, third order polarization effects could be induced through the interaction of the second harmonic and the fundamental frequency. Furthermore, in semiconducting samples, such as monolayer TMDCs, it is possible to excite above the bandgap of the material. This above-bandgap illumination then causes electrons to be excited from the valence band to the conduction band of the material, leading to free charge carriers. At the surface, these carriers are known as surface photo-voltage (SPV), and in semiconductors they cause a measurable force on the AFM tip due to band bending [26]. The magnitude of this force is linearly dependent on the power of the incident light, and increases when a bias is applied between the tip and the sample. Thus, the forces caused by SPV can be distinguished from nonlinear polarization by comparing the power and bias dependence of the AFM signal.

2.4 Noise

In addition to disentangling the various sources of signal in this system and understanding the impact of the AFM on these mechanical measurements of optical phenomena, it is also very useful to study the noise in the system.

For one, understanding noise is crucial to optimizing an experiment and extracting as much information as possible. In fact, in this experiment the noise could potentially become the measurement itself. Currently, the area within which a material's $\chi^{(2)}$ may be measured is limited by the amount of time it takes to take the data. To achieve a good signal to noise on the autocorrelation measurement, it is often necessary to take many data points and average for a long time at each one, leading to autocorrelation measurement times on the order of minutes. This long time scale is very limiting when it comes to taking a grid of autocorrelations, as the instrument has a slow drift that becomes significant for measurements taking many hours. One method of overcoming this limitation is to extract the $\chi^{(2)}$ value from the noise in frequency signal at a given delay time.

In general, Figure 2.5 shows that the noise in the frequency shift increases dramatically at delay times close to zero. Here, time traces show strong fluctuations at zero time delay and a much smaller standard deviation at time delays far outside the coherence length.

This increase in noise may potentially be attributed to a few different sources. For example, it could be the result of fluctuations in the delay between the interferometric arms, which would lead to large fluctuations in intensity around zero time delay due to the large fringe amplitude there. However, optical measurements of the autocorrelation do not show the same increase in noise around zero delay as shown in Figures 2.5 and 2.6, making it unlikely that this is the source of the noise. Alternatively, the noise could be the result of the increased intensity of the light at the central fringe. This light intensity may result in single photon interactions within the material, which cause a fluctuating AFM signal. More work is needed to distinguish these noise sources.

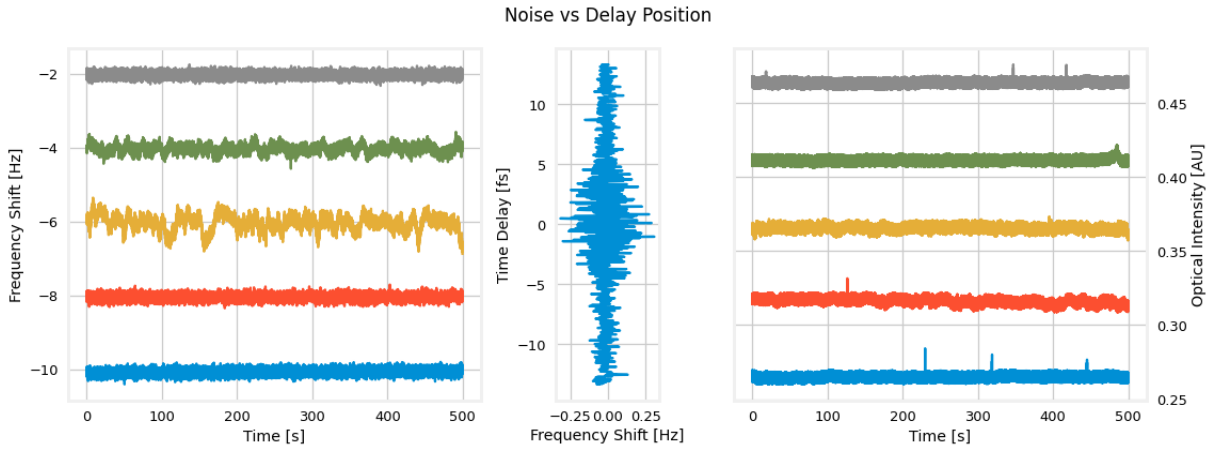

Figure 2.5: Time traces show a significant increase in the noise on the frequency shift signal (left) at time delays close to zero, with little change to the optical signal noise (right). The central plot shows an example of an autocorrelation measurement. In the left and right plots, the measurements are shifted on the y-axis for easy of visualization. Both the frequency shift and optical intensity traces were taken with a sample period of 20ms and the frequency shift data was taken at a setpoint to -10Hz and a cantilever oscillation amplitude of 6nm. Long z-feedback was used to account for slow drifts with a gain of 50pm/Hz and a time constant of 150ms.

The noise on the AFM signal was also measured as a function of the incoming light power. At the central fringe, the standard deviation of the frequency shift was found to increase dramatically with light intensity, as shown in Figure 2.7. This increase shows a jump around a normalized intensity of 0.8, which may indicate a threshold behavior. However, the variation in the noise is also approximately quadratic. Such a quadratic relation would be expected if the source of the noise was a nonlinear optical effect as discussed in Section 2.3. Simultaneously, the noise was constant far from the fringe pattern. In this regime, the pulses from the etwo beams are not overlapping, so one would not expect to see any difference frequency generation causing a polarization. However, the individual beams should still be interacting with themselves leading to optical rectification as described in Section 1.2. The lack of variation in the noise in this regime as a function of intensity thus suggests that the optical rectification does not strongly contribute to the noise. It also suggests that the noise is unrelated to heating effects in the

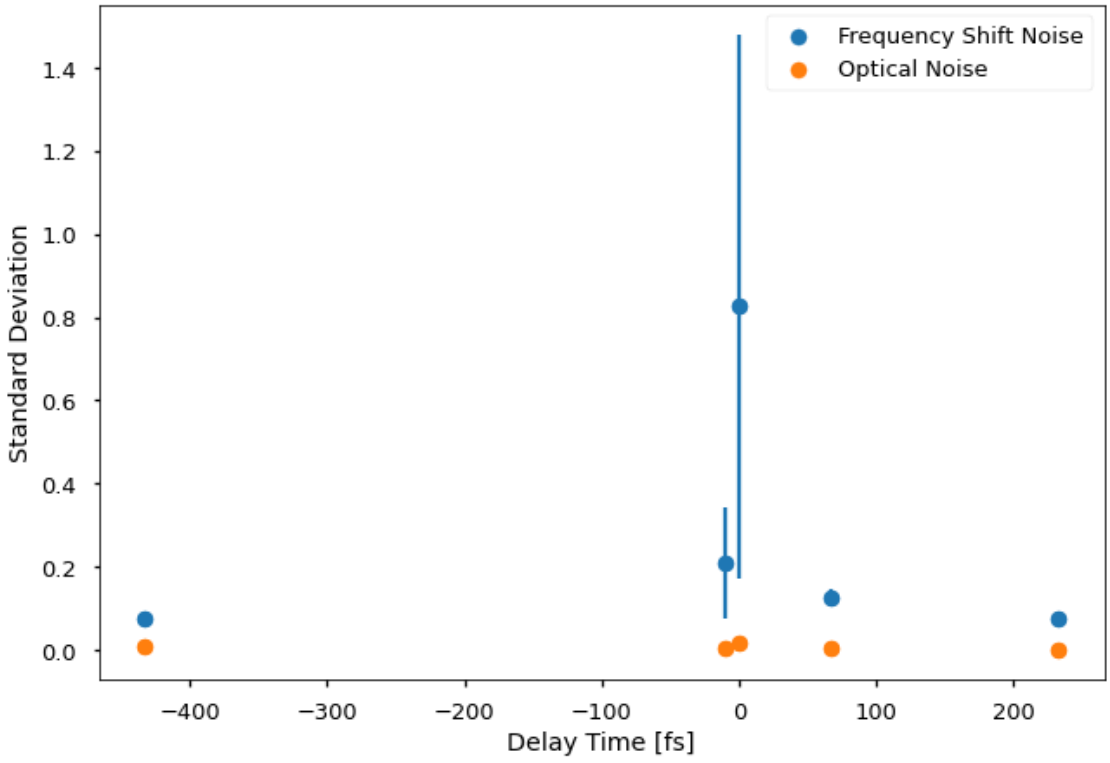

Figure 2.6: Standard deviation in the frequency shift signal and optical intensity as a function of time delay. At long delays, the two noise levels approach one another. The frequency shift noise data was taken at a setpoint of -10Hz with an oscillation amplitude of 6nm. The z-feedback was slow, with a proportional gain and time constant of either 10pm/Hz and 250ms or 50pm/Hz and 150ms. Both the frequency shift and optical noise was measured with a sample period of 20ms and the laser power was 140mW for all measurements.

tip-sample junction, since these should also be intensity dependent even outside of the autocorrelation fringe pattern.

Thus, the noise on the AFM signal, which varies significantly with time delay and light power, can most likely be attributed to a difference frequency generation effect. This opens the door for the possibility of measuring the $\chi^{(2)}$ of a material without having to run a full autocorrelation scan, allowing for faster measurements and larger scan areas in the future.

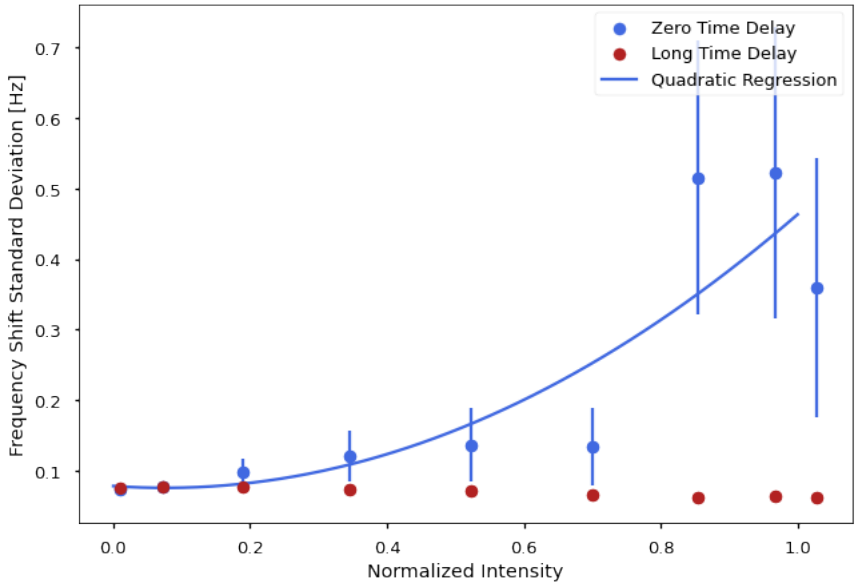

Figure 2.7: Standard deviation of frequency shift noise as a function of light intensity. At short time delays, the frequency shift noise increases with power, while at long time delays of about 433 fs the noise is constant. The intensity-dependent increase in noise around zero delay is approximately quadratic, though more data is needed to confirm this relation. The frequency shift noise was measured at a setpoint of -10Hz and a cantilever oscillation amplitude of 6nm. Slow z-feedback with a gain of 40pm/Hz and a time constant of 50ms was used.

Chapter 3

Tungsten Disulfide

3.1 Material Choice

As discussed in Section 1.1, monolayer TMDCs are scientifically interesting materials which also typically display large nonlinear susceptibilities, and for this experiment, a material with a high second-order nonlinear susceptibility is preferred, as a higher $\chi^{(2)}$ will yield a larger measurable signal. The literature values for two commonly studied TMDCs, MoS_2 and WS_2 are summarized in Tables A.1 and A.2, though these measured and modeled susceptibilities vary widely as a function of preparation methods, modeling uncertainties, and wavelength.

To experimentally determine the non-linear susceptibility, many studies focus on second harmonic generation, as the SHG intensity can be linked to the second-order susceptibility by Equation 1.13. The connection between these two values, however, can be modeled with varying degrees of complexity, so it is important to note which assumptions are being made in a given study. For example, there is a relatively small group of papers studying MoS_2 that report $\chi^{(2)}$ values about three orders of magnitude higher than other literature [5,27,28]. Clark et al. showed that this "three orders of magnitude discrepancy" can be accounted for by modeling the material as a bulk rather than a sheet [29]. Thus,

the model used to calculate the second-order nonlinear susceptibility from measurable intensities is incredibly important.

The second-order susceptibility is also strongly dependent on the excitation wavelength. In order to understand this dispersion, it is useful to look first at the reflectance and/or transmission spectra of the material, such as monolayer WS_2 (or MoS_2). As shown in Figure 3.1 [30], the reflectance spectrum of WS_2 varies as a function of the number of layers, but its general shape remains constant. In this shape, the three main exciton peaks of WS_2 can be clearly identified and are labeled A, B, and C by convention. The peaks originate from direct optical transitions at the K (for A and B) and Γ (for C) points of the Brillouin Zone [25]. Literature values for these WS_2 exciton energies are summarized in Table B.1.

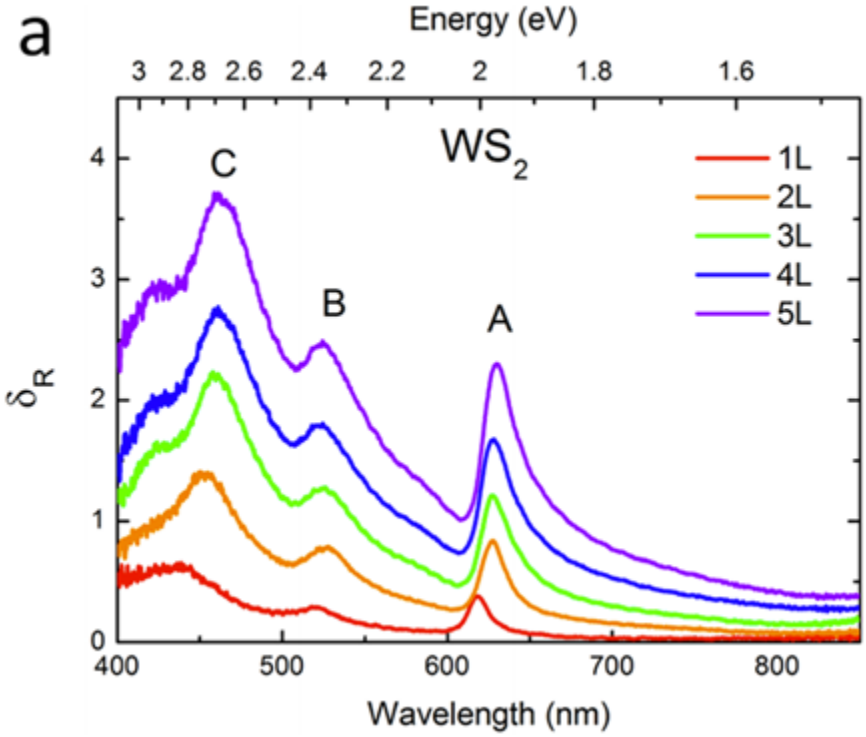

Figure 3.1: The reflectance spectrum of exfoliated WS_2 as a function of layer number, as measured by Zhao et al. [30]. The A, B, and C exciton peaks are clearly visible and shift slightly as the number of layers decreases. This shift can be attributed to the change in the chemical environment as a function of layer number.

In general, second harmonic generation intensities and nonlinear susceptibilities show resonant excitation effects near these exciton peaks, likely due to an increased density of states at these points in the Brillouin Zone [25, 28]. Thus, the lowest $\chi^{(2)}$ values are reported in the static limit, far from any exciton peaks while the highest values are typically found near the high energy C peak. From the values reported in Tables A.1 and A.2, WS_2 was found to have the largest peak non-linear susceptibilities and was therefore chosen for this experiment.

Interestingly, DFT studies of WS_2 have predicted an even larger nonlinear response at energies above the C exciton, with a peak at an excitation wavelength of 600 nm as shown in Figure 3.2 [31]. Though these theoretical predictions have not yet been verified experimentally, it is likely that the nonlinear response of WS_2 will, on average, be larger at shorter excitation wavelengths than longer ones.

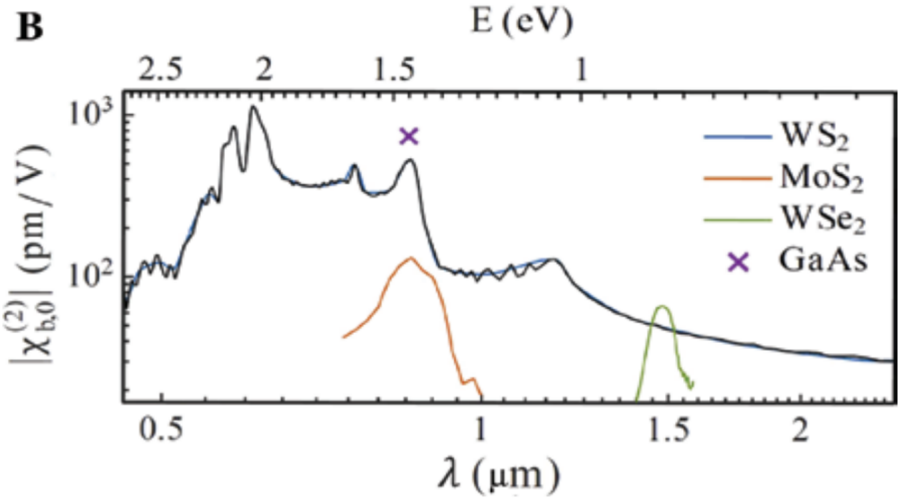

Figure 3.2: Review of DFT simulations of the $\chi^{(2)}$ dispersion for various TMDC monolayers as well as GaAs, which is often used as an ultrafast modulator [32]. For WS_2, the dispersion shows particularly high theoretical values at short wavelengths. Figure adapted from [31, 33].

3.2 Sample Preparation

Monolayer samples of TMDCs such as WS_2 can be prepared through a variety of methods. In general, these can be separated into two categories: top-down exfoliation methods and bottom-up growth methods. Exfoliation methods such as liquid or mechanical exfoliation typically result in higher quality flakes with fewer defects and a monocrystalline structure [34], while growth methods like chemical vapor deposition (CVD) are able to produce much larger samples but are typically plagued by defects and a polycrystalline structure that leads to reduced transport properties [34, 35].

Sample preparation techniques may also have a large effect on the nonlinear response of the monolayer WS_2 as illustrated in Table A.2. A large part of the discrepancy in the measured $\chi^{(2)}$ values, even at the same wavelength, can likely be attributed to defects introduced by varying sample preparation techniques.

In this work, both mechanically exfoliated and CVD-grown WS_2 samples were investigated.

3.2.1 Mechanical Exfoliation

First, few-layer flakes of WS_2 were exfoliated mechanically from a bulk crystal. Generally, this mechanical exfoliation process looks slightly different for each individual researcher. For this work, a simple scheme shown in Figure 3.3 was used. Specifically, flakes of WS_2 were picked up from the bulk crystal using Nitto tape (SPV-224PR-MJ). This tape was chosen because it is less sticky than traditional Scotch tape and is therefore expected to be gentler and leave less residue on the sample. Then, the tape with the WS_2 taken directly from the bulk crystal was stuck to a second piece of tape. The two attached pieces of tape were rubbed gently and carefully pulled apart to facilitate the transfer of layers of WS_2 to the new piece of tape. This procedure was repeated using up to 20 pieces of tape until the WS_2 was barely visible on the tape.

The final piece of tape was then stuck to a small piece of silicon topped with 285 nm of silicon oxide (SiO_2). This specific substrate was chosen because it provides a particularly good background for initial optical identification of monolayers [36,37]. This is believed to be due to interference effects from the transparent layer of SiO_2 [38,39].

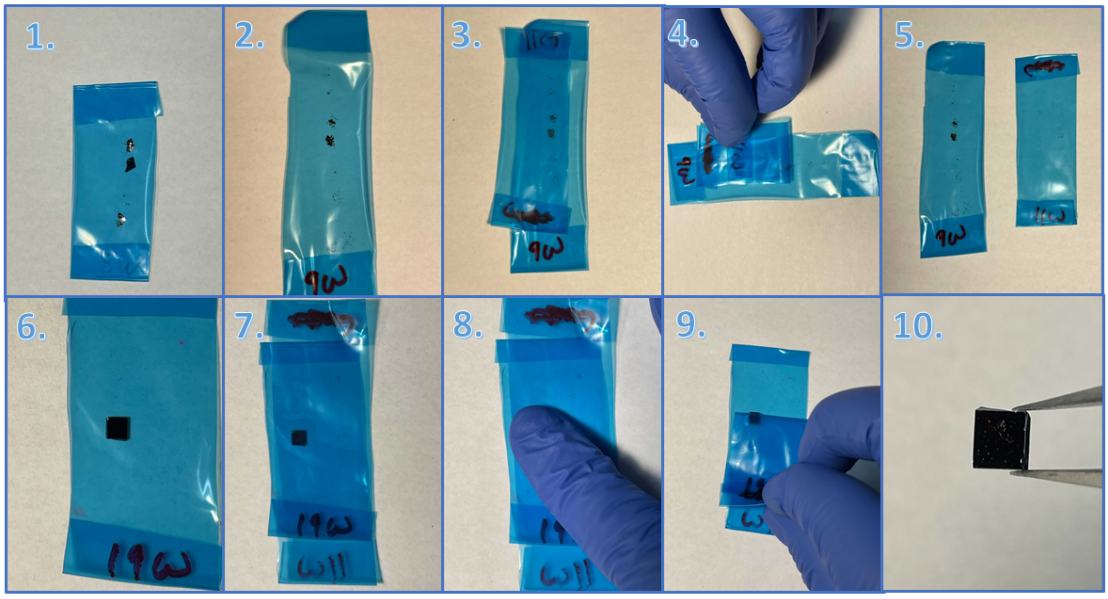

Figure 3.3: WS_2 flakes were exfoliated from a bulk crystal using blue Nitto tape. Large pieces were first transferred from the bulk crystal to a piece of tape (1, 2). Then, a clean piece of tape was stuck to the first and peeled off again to transfer some of the WS_2 crystal (3-5). Steps 3-5 were repeated until the WS_2 was barely visible on the tape. Then a cleaved piece of SiO_2 was placed on a fresh piece of tape (6). The tape with the WS_2 flakes was then stuck to the SiO_2 substrate and gently rubbed to encourage transfer of the flakes before being peeled off again (7-9). The sample (10) was then characterized with an optical microscope to determine if there were few- or single-layer flakes present.

The flakes now on the silicon substrate were then characterized first using an optical microscope and then using tapping mode AFM in air. The resulting images shown in Figure 3.4 were taken using a Nanoscope MultiMode SPM. Using this method, flake heights were measured to be on the order of 3-13 nm. This indicates that monolayer flakes were likely not achieved using this method.

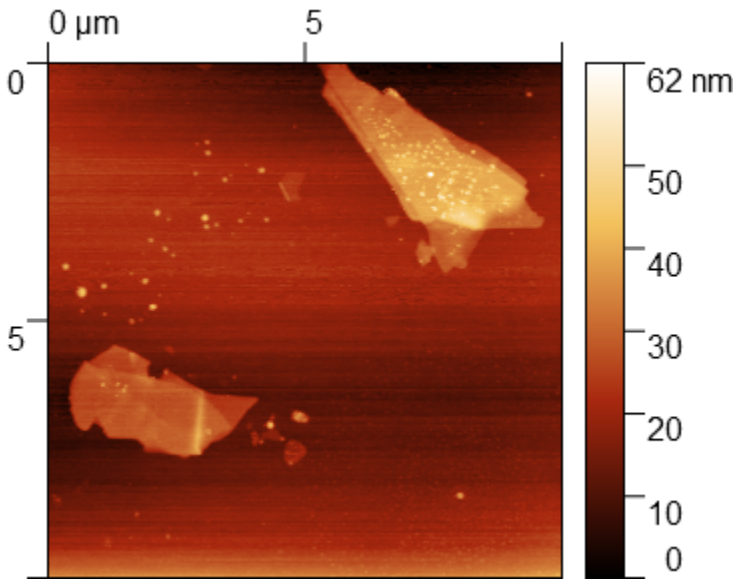

Figure 3.4: Mechanically exfoliated WS_2 flakes. The thinnest regions have heights between three and thirteen nanometers. Image were taken in air using tapping mode AFM on a Nanoscope MultiMode SPM. The cantilever drive frequency was 67.5kHz with a drive amplitude of 1.621V. The free oscillation amplitude was 1V and the setpoint used was 550mV.

Importantly, one of the main downsides of mechanical exfoliation is the limited flake size. While more complex exfoliation methods than the one attempted here have been shown to be capable to reliably producing monolayer TMDC samples [34, 37, 40], the density of these flakes is relatively low. On a 2x5 mm substrate, one might expect to find only one or two monolayer flakes which have sizes on the order of microns. Due to the lack of optical access in the UHV-AFM system, finding such flakes has therefore proved to be particularly difficult.

3.2.2 Chemical Vapor Deposition

In contrast to mechanically exfoliated flakes, monolayer TMDCs grown using chemical vapor deposition (CVD) can uniformly cover much larger, even wafer-scale, areas. This makes them promising for characterization in the UHV-AFM system, where positioning and searching capacities are limited.

CVD is a process whereby thin layers of materials are grown on a surface. Specifically, a vapor is introduced into a chamber containing a substrate, which is typically heated. Through a chemical reaction at the surface of this substrate, solid material is then deposited [35, 41]. The physical and chemical properties of the resulting material can be tuned by adjusting experimental conditions such as the substrate material and temperature, the composition of the reaction gas, the total pressure, and gas flow rates. In general, this technique is very useful for creating large-scale, uniform thin films [41].

When it comes to producing monolayer TMDCs, CVD-based techniques are often favored, as they are capable of covering large areas which will be necessary for large-scale device manufacturing in the future. However, these CVD-grown monolayers typically exhibit a higher density of defects than exfoliated, top-down, samples. Generally, because there are many nucleation sites, a poorly controlled growth process can easily result in a large number of grain boundaries and corresponding defects as individual flakes grow together [34, 35]. For example, when TMDCs are grown on top of other van der Waals materials, such as graphene, there is no energetic difference between 0° and 60° oriented flakes. As these grow together, inversion domain boundaries are formed, which are metallic and result in conducting channels in the monolayer semiconductor [35]. Other substrates, such as sapphire, have been used to overcome these inversion domain boundaries, but have resulted in different defects, for example from flakes growing together that are misaligned by less than a lattice spacing [35]. In addition, CVD-grown WS_2 is know to oxidize over the course of weeks in ambient conditions [42]. This oxidation, which has been attributed to photo-oxidation effects, results in additional defects at the flake edges and along strain axes [42]. Nonetheless, it is useful to study the nature of these defects and their effects on the sample's linear and nonlinear optical properties.

In this work, CVD-grown WS_2 samples grown in the group of Johnson Goh at the National University of Singapore were characterized first using x-ray photoelectron spectroscopy (XPS). The results of this analysis, displayed in Figure 3.5, showed that after transport, the chemical makeup of the flake was dominated by partially oxidized tung-

sten, WO_2, with only a small feature from WS_2. Additional spectra are provided in Appendix C. The flakes were subsequently imaged in ambient, tapping mode AFM using an Asylum MFP-3D SPM microscope. They exhibited a number of interesting behaviors and characteristics which will be discussed in depth in Section 3.3.

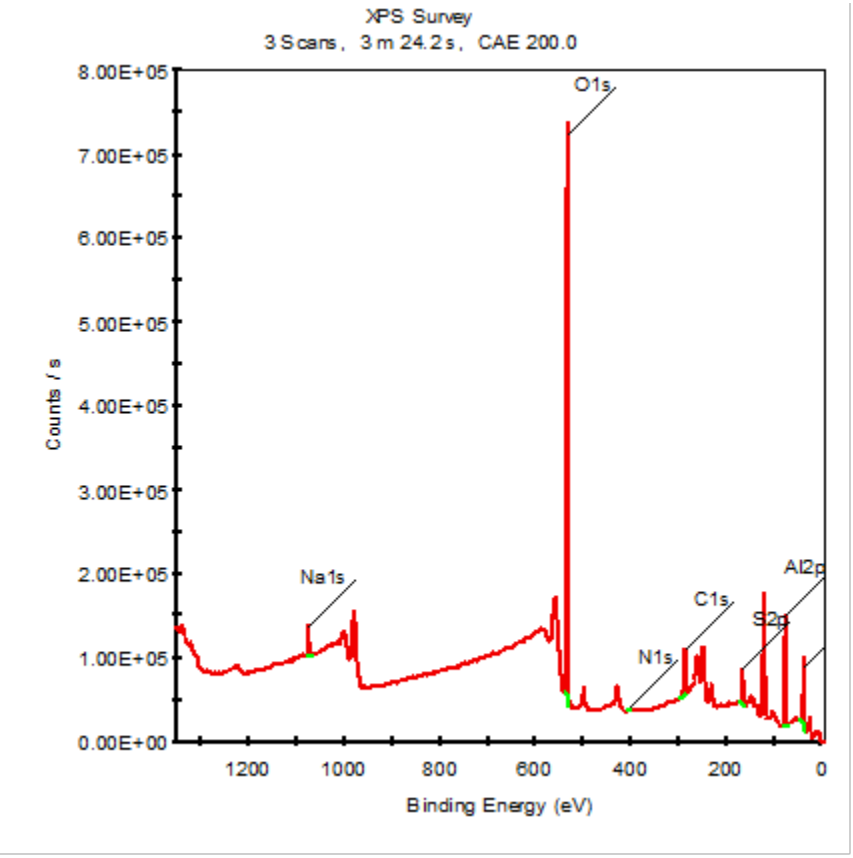

Figure 3.5: X-ray photoelectron spectrum of CVD-grown WS_2 flakes. The sample was found to contain 3.91% sulphur and 1.92 % tungsten, as well as 48.47% oxygen as summarized in Table C.1. The main tungsten peak is W_4^+, which is typical for partially oxidized WO_2, though there is also a small peak from WS_2 around 33eV, which can be seen more clearly in Figure C.3. This data was taken using an Al K Alpha source gun with spot size of $400\mu m$.

3.3 Photo-oxidation and Charge Storage

Though it is useful to study pure samples with few defects in order to fundamentally understand the behavior and nature of TMDCs, it is often impractical to produce such 'clean' samples, especially on large scales. In addition, samples with many defects, grain boundaries, and even oxidation may exhibit particularly interesting and technologically relevant behaviors. This is true for the CVD-grown WS_2 flakes described in Section 3.2 and measured in this work.

After growth, the WS_2 flakes were expected to exhibit a height above the sapphire substrate between 1 and 2 nm, corresponding to the three layers of atoms as shown in Figure 1.1 in addition to the bond length between the substrate and the monolayer. However, when the flakes were imaged using tapping mode AFM after shipment across the Pacific ocean, they exhibited extraordinarily tall topography between 40 and 60 nm as well as broad steps with widths on the order of 1 micron at the edges of flakes as shown in Figure 3.6. This unusual behavior persisted in a newly grown second sample as shown in Figure 3.7.

In order to accurately interpret these tapping mode topography images, it is important to remember that atomic force microscopes are sensitive to all forces acting between the tip and the sample and trace contours of constant force. In this case, it was assumed that non-topography contributions to the force would be negligible, so all information measured by the AM-AFM were attributed to topography and flake heights. However, this assumption turned out to be false. Both the significantly too tall step heights and the width of the steps themselves are evidence for the idea that electrostatic forces played a large role in the images shown in Figures 3.6 and 3.7.

To test this, a benchtop air ionizer (3M 963E), which is intended to be used to dispel static electricity, was used to direct ionized air at the sample and discharge any charges trapped on the flakes by the insulating substrate. In the wake of the deionization, the WS_2 flakes were once again measured in air with tapping mode AFM. The results, shown in

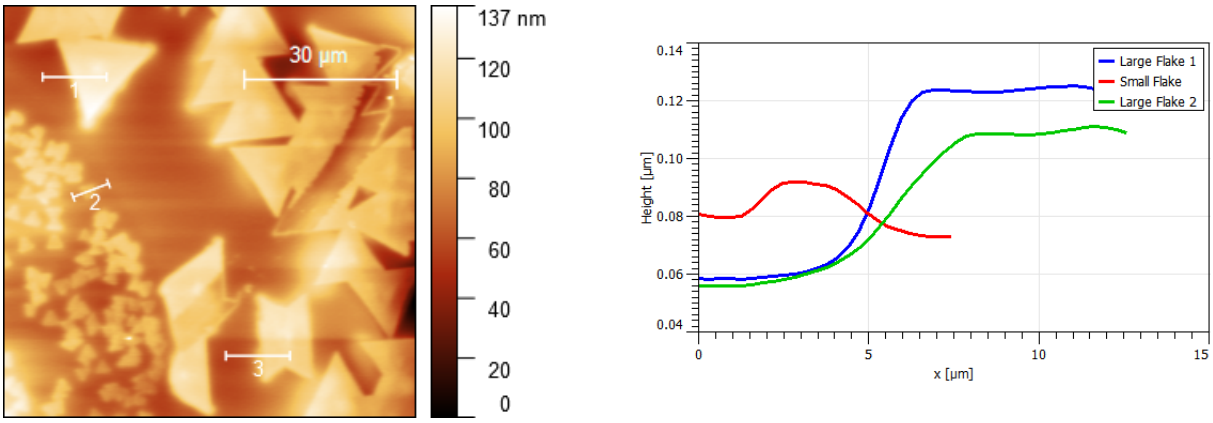

Figure 3.6: Topography of CVD-grown WS_2 flakes measured using tapping mode AFM in air (left). The flakes exhibit very large step heights between 10nm and 60nm as illustrated by the line traces shown on the right. These tall and broad steps can be attributed to strong electrostatic forces between the flakes and the AFM tip. A tip with a force constant of 2N/m was used with an amplitude of 57.6nm, a drive amplitude of 20.7mV, and a drive frequency of 66.8kHz. A 0.51Hz scan rate was used.

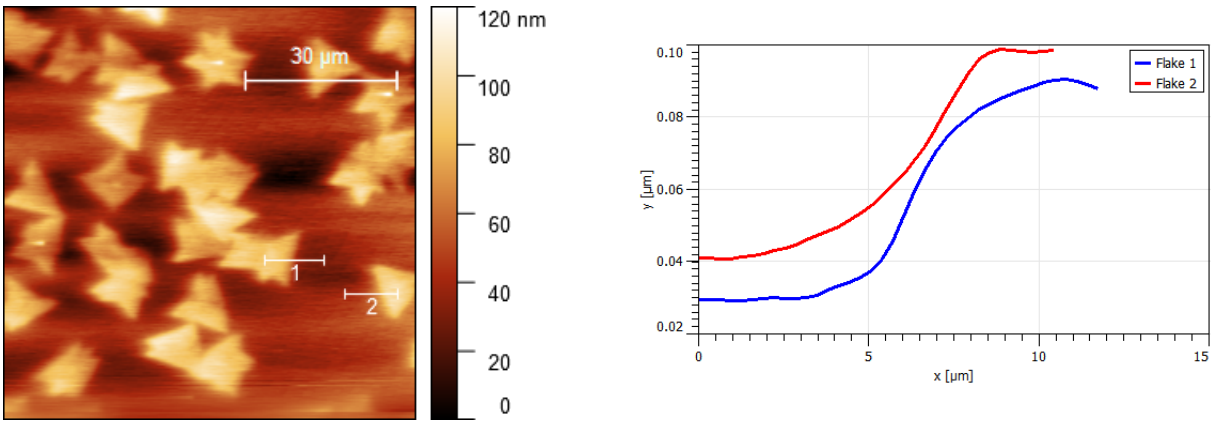

Figure 3.7: A second CVD-grown WS_2 sample continued to exhibit large step sizes on the order of 50 to 60nm. The topography, imaged using tapping mode AFM in air is shown on the left, while line profiles of two different flakes are shown on the right. The AFM image was taken using a 2N/m tip with a free oscillation amplitude of 109nm, an amplitude setpoint of 65.4nm, and a scan rate of 1.07Hz. The cantilever was driven at a frequency of 69kHz with a drive amplitude of 29.8mV.

Figure 3.8, showed flakes with heights of a few nanometers and sharp step edges. Thus, it was clear that the CVD-grown flakes had become charged during transport.

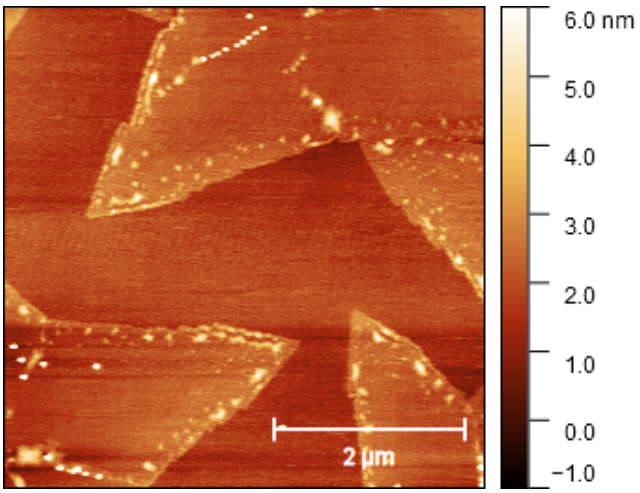

Figure 3.8: Image of CVD-grown WS_2 flakes after discharging with a de-ionizing bench-top fan. Flake heights are between one and two nanometers and one can clearly see the presence of oxidation and other defects at the edges of the flakes and along the crystallographic axes. This image was taken using tapping mode AFM in air with a free oscillation amplitude of 109nm and an amplitude setpoint of 83.7nm. A scan rate of 0.89Hz was used and the cantilever was driven at 67.5kHz with a drive amplitude of 50.7mV.

The next goal was then to understand the mechanisms by which this charging occurs and, importantly to investigate the relevant time scales. For example, the samples remained charged over the course of weeks until they were discharged manually, so the ability to store charge over long time periods was especially interesting.

Firstly, the sample behavior was investigated as a function of illumination. It was found that, under white light illumination, the tip-sample interaction forces over the flakes were much higher as shown in Figure 3.9. In fact, the sign of the measured step heights changed from -8nm to +15nm, which equates to a change of 33nm. In addition, the sample was also illuminated using an LED light source with a central wavelength of 565nm. The flakes exhibited a similar 'growth' under this short wavelength illumination, with step heights growing from about 1nm to about 8nm as shown in Figure 3.10, though there was no reversal of the direction of the step.

The increase in tip-sample interaction forces under illumination can be attributed to an increase in electric charges on the WS_2 flakes. These charges may be, for example,

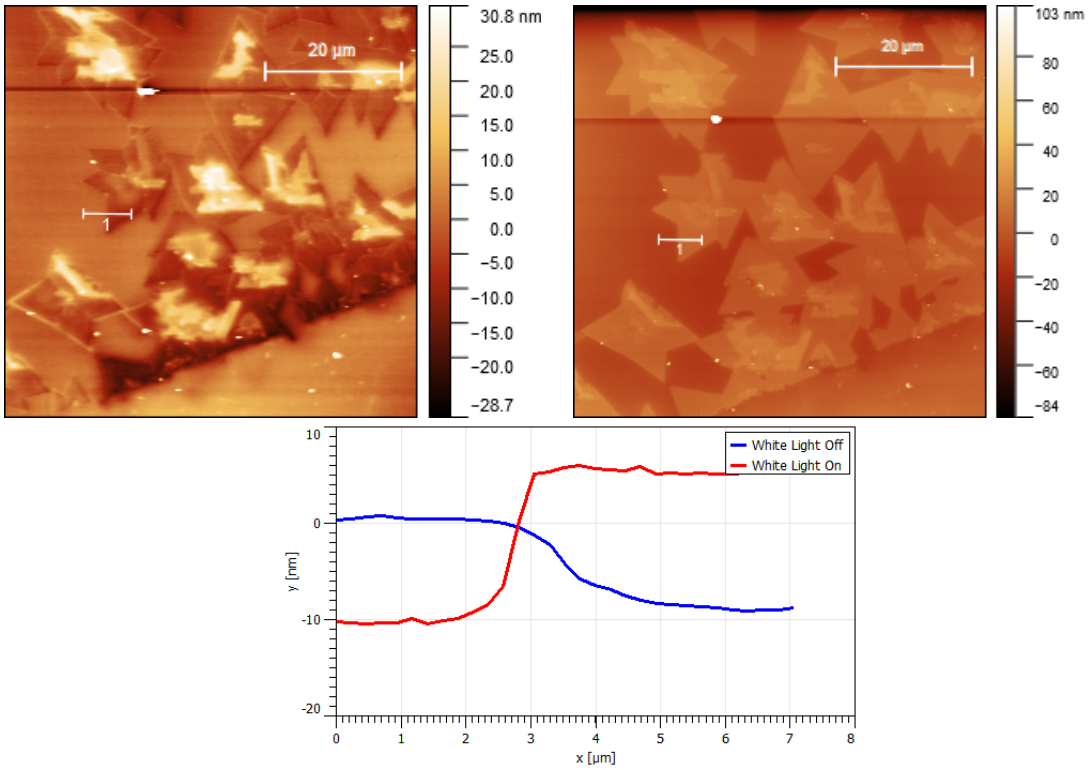

Figure 3.9: CVD-grown WS_2 flakes in the dark (left) and under white light illumination by a halogen lamp (right). The line traces (bottom) show that the measured step heights change from negative to positive after illumination. This drastic change indicates that the signal arises not from real topography, but rather from strongly light-dependent electrostatic forces in the flakes. Both AFM images were taken with a free oscillation amplitude of 109nm and a setpoint of 72.7nm at a scan rate of 0.7Hz. The cantilever was driven at 70.05kHz with a drive amplitude of 114.7mV.

the result of electrons excited from defect states in the flakes. Alternatively, they may be attributed to charges transferring from the substrate to the flake. In this case, the relevant energy scale for the illumination is not the bandgap of the WS_2 but rather than band offset between the sapphire substrate and the flakes. Determining the exact origin of the charging behavior will require additional modeling and careful checking of the sample preparation technique. Sapphire substrates are usually -OH terminated, but annealing leads to a loss of the OH and subsequent aluminum enrichment at the surface [43]. It is possible that this layer of aluminum acts like a capacitor to trap the electrons, but a

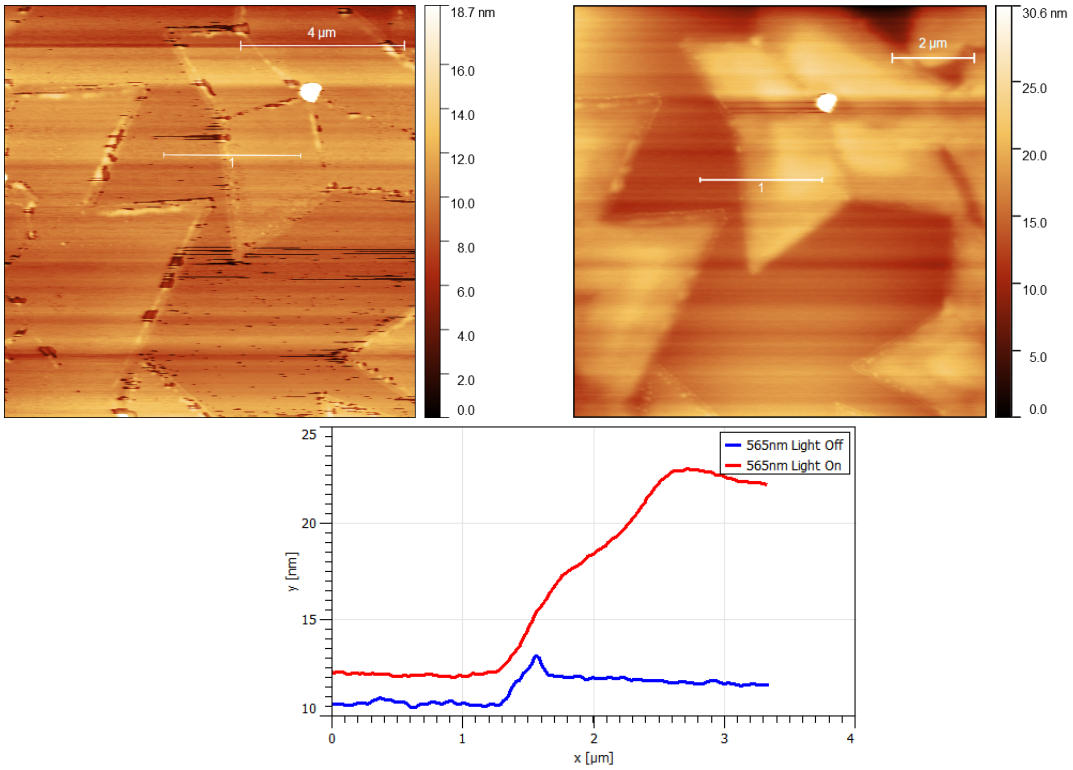

Figure 3.10: With 565nm wavelength illumination (off=left, on=right), the CVD-grown flakes grow from about 1nm to about 12nm in height indicating the continued presence of strong light-dependent electrostatics at short wavelengths. In addition, clear regions of charge build-up in the interior of the flakes emerge upon illumination. Both AFM images are taken with a free oscillation amplitude of 109nm and an amplitude setpoint of 76.4nm. A scan rate of 1Hz was used and the cantilever was driven at 70.1kHz with a drive amplitude of 46.7mV.

DFT model will be necessary to investigate which states are localized where. In general, a better understanding of the effects of the sample preparation process will allow for more detailed models and a better understand of the charge trapping mechanisms in this sample.

It is also interesting to note that the images of the flakes under illumination also show distinctive triangular patterns centered around the nucleation site, which indicate that this phenomenon occurs differently at the edges of the flakes and grain boundaries than at the center. If oxidation of the flakes contributes to the charging mechanism, this would

makes sense, since there is a clear increase in oxidation and other defects at these boundaries.

In addition to the charging mechanism, it is also useful to investigate the behavior of the charges over time. For example, after illumination, the flakes were found to discharge slowly over multiple hours. Figure 3.11 shows a series of images taken over the course of five hours. As time goes on, the step heights between the flake and the substrate grow smaller and individual defects emerge as can be seen in Figure 3.12, which shows topography line traces over time at four different locations. During this time, the step heights drop from about 12nm to less than 1nm, as shown in Figure 3.13.

In addition, lines of individual defects emerge along the crystallographic axes. These are especially clear in the bottom right corner of the later images, since the longer-range electrostatic forces in the earlier images make it difficult to resolve them. The long time scales of this charge decay point to promising future applications of such a material for charge storage. However, a more thorough investigation of how this decay time varies with illumination and environment will require additional modeling and measurements in order to reproduce the observed sample properties and take advantage of this unique mechanism.

Finally, to understand the charge separation in this system, multi-pass Kelvin probe force microscopy, or KPFM, was performed. In this measurement technique, the cumulative tip sample forces are measured over a line scan. Then, while the tip is passed over the same line along this contour of constant force, a bias is applied between the tip and the sample to null electrostatic interactions. This allows for the extraction of the electrostatic component of the tip-sample interaction force.

For this sample, the surface potential measured by KPFM is shown in Figure 3.14. As expected, there is a clear difference between the substrate (light) and the flakes themselves (dark). In addition, there is contrast along the grain boundaries within the flakes themselves and along their edges. The increase in electrostatic potential at these grain boundaries indicates an uneven charge distribution within the flake that could be indica-

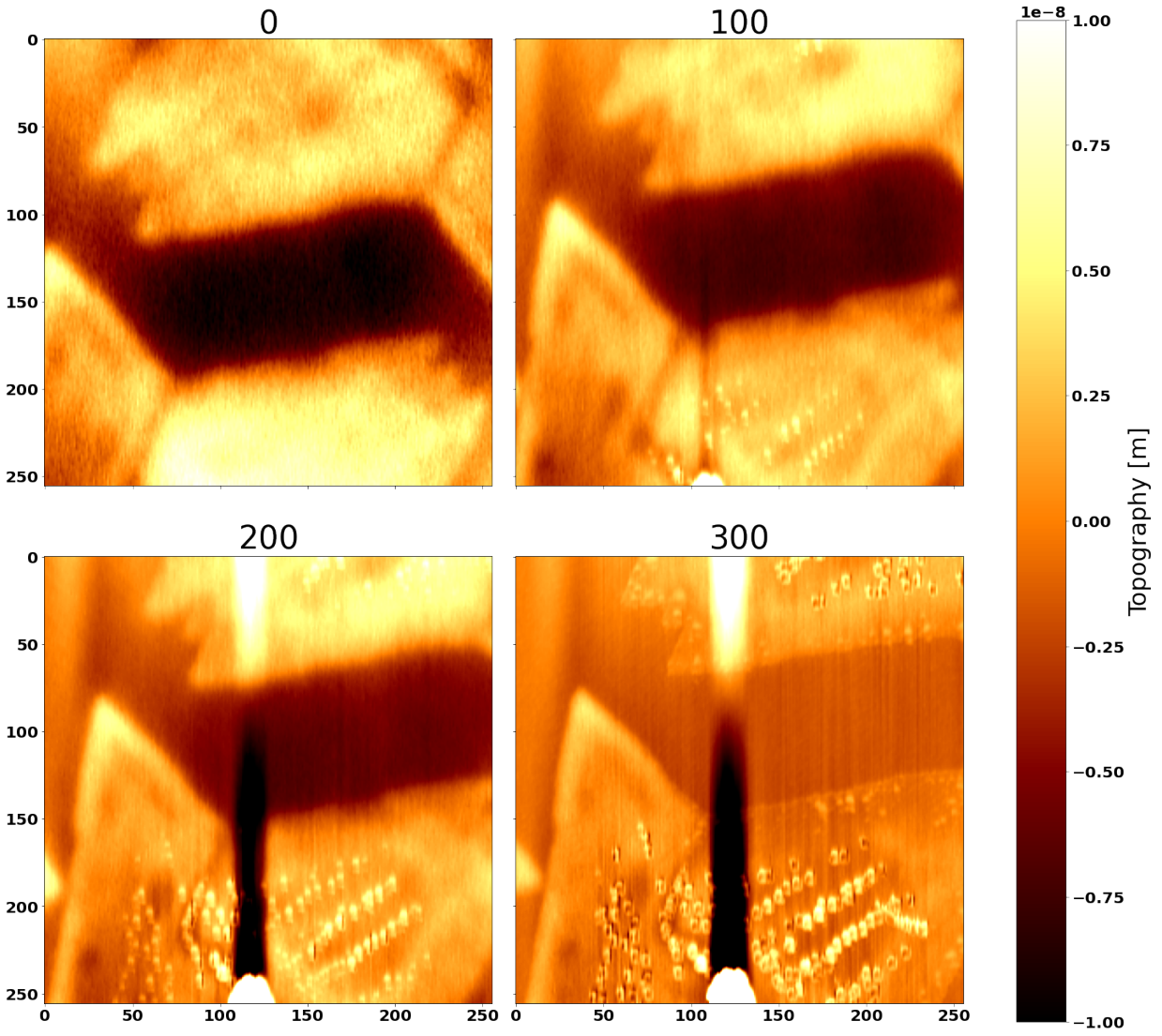

Figure 3.11: Topography of the charged CVD-grown flakes over the course of about four hours. Each image is labeled by the number of minutes elapsed since the first scan. As time progresses, the step height decreases and individual defects become visible. This is likely due to a slow charge dissipation which leads to less tip-sample interaction and more localized force detection over time. The slow drift of the microscope in the -y direction is also clearly observable and a vertical stripe appears in later images, caused by a defect along the bottom edge drifting into frame. Images are taken with a scan rate of 1Hz and an amplitude of 73.5nm. The cantilever was driven at 70kHz with a drive amplitude of 36.7mV.

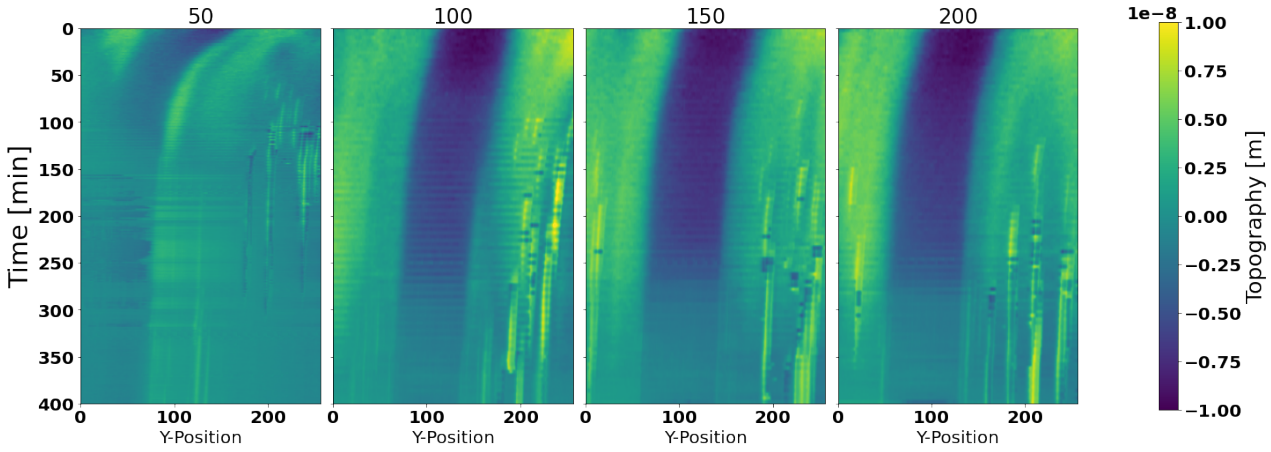

Figure 3.12: Line traces at four different flake locations over time. The x-axis shows the tip position along the line scan, while the color map shows the measured topography. The time scale on the y-axis spans 6.67 hours from top to bottom, and each plot is labeled by its x-axis location in the topography images shown in Figure 3.11. Over time, The step size decreases and sharp, bright defects emerge as bright stripes in the color maps.

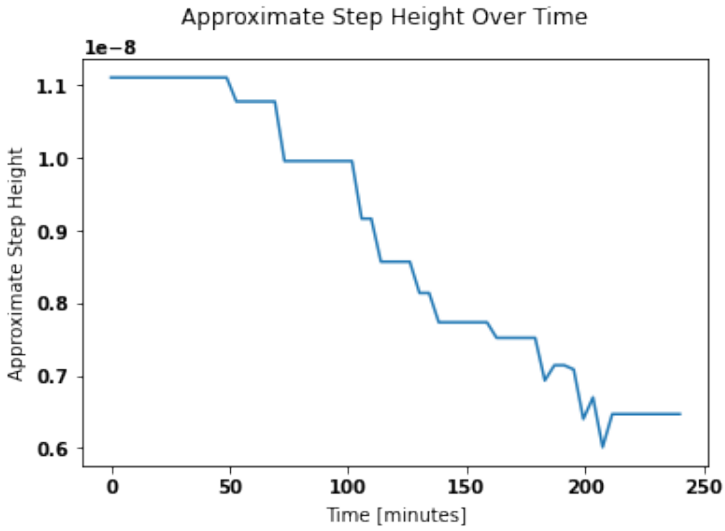

Figure 3.13: The measured height of the flakes decreases over the course of about four hours as the flakes slowly discharge. The decay time is on the order of hours, but more data and better fits will be required to determine an exact time constant. The flake heights were extracted from the topography shown in Figure 3.11 by fitting two Gaussian functions to histograms of the topography and finding their relative positions.

tive of the charge separation mechanism necessary for producing the long charge decay observed in this sample. Thus, KPFM imaging of these oxidized WS_2 flakes shows a potential landscape within the sample that could lend itself to charge accumulation and separation.

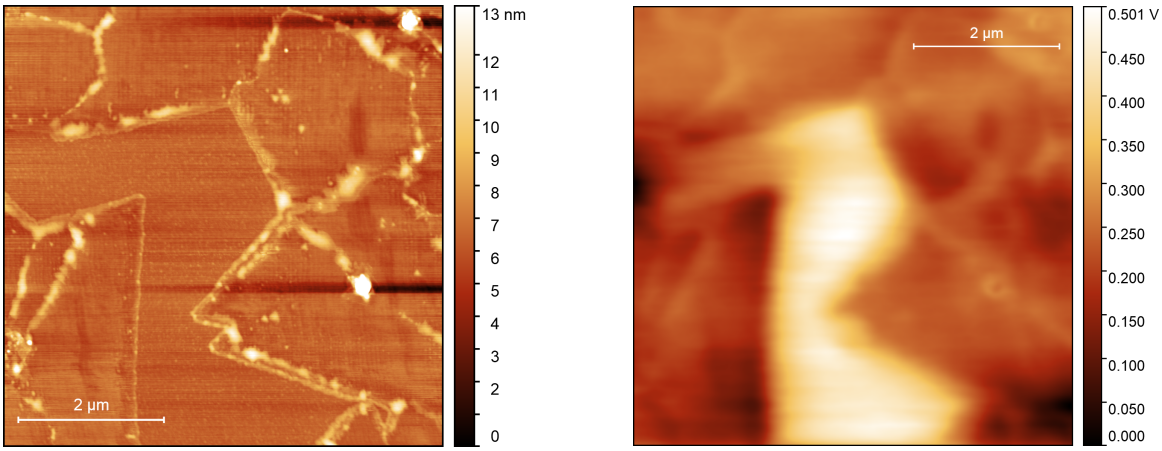

Figure 3.14: Topography (left) and electrostatic potential (right) of the CVD-grown WS_2 flakes measured using multi-pass KPFM. The potential landscape of the flakes correlates well to the flakes and shows contrast along grain boundaries and at the edges of the flakes. In contrast to the substrate, a larger negative bias is applied to the tip over the flakes, indicating the presence of more holes or other positive charges in these regions. For these images, an amplitude setpoint of 65.4nm from the free oscillation amplitude of 109nm was used. In addition, the scan was performed very slowly, at a rate of 0.07Hz, and the cantilever was driven at 68.9kHz with a drive amplitude of 390mV. For the KPFM passes, a constant offset of -65nm relative to the average cantilever position was used.

Overall, the CVD-grown WS_2 flakes studied in this work exhibited strong charging behaviors that were illumination-dependent and had long decay time scales, but could be discharged relatively easily using ionized air. These characteristics are potentially very useful in optoelectronic applications, but require closer consideration, especially through modeling of the substrate and local environment, will be necessary before they can be understood, reproduced, and applied.

Chapter 4

Conclusions

4.1 Summary

Optically pumped atomic force microscopy represents an exciting new technique for investigating the optoelectronic properties of surfaces and novel, thin-film materials. In this work, its potential for measuring nonlinear optical susceptibilities was highlighted.

Specifically, the technique was first tested using a thin film of the merocyanide dye HB238. This material is known to have a large dipole moment and exhibit strong optical nonlinearities, making it an ideal candidate for studying the origin of the optically-pumped AFM signal. Ultimately, it was found that the amplitude of an autocorrelation function measured with the AFM varies quadratically with power. This confirms that the signal originates from a nonlinear process, as anticipated.

Additionally, the noise in the frequency shift signal was characterized. This noise was found to increase dramatically at interferometer delay times close to zero. The origin of this increase is not clear. It could be caused by the increased intensity of the light at the central fringe leading to single photon interactions within the material. Alternatively, the increased noise amplitude could be due to instabilities in the delay line, though the optical signal did not show a corresponding increase. In addition, the noise intensity at the central fringe was found to increase approximately quadratically with the power of the in-

cident light, implying that it is at least in part related to a nonlinear optical phenomenon. Overall, however, the noise is not yet reliably correlated with the signal strength, so more work will be necessary to determine what information can be extracted from the frequency shift fluctuations.

Alongside characterizing the measurement technique, the other goal of this work was to use the optically pumped AFM to investigate the properties of single- and few-layer transition metal dichalcogenides, specifically WS_2. In order to achieve this goal, flakes of WS_2 were manufactured both through mechanical exfoliation and chemical vapor deposition. Though they require less specialized equipment to produce, the mechanically exfoliated flakes were exceptionally difficult to localize in the UHV-AFM setup used here, making them impractical to measure without an additional imaging technique, such as SEM. In contrast, the CVD-grown flakes were easier to locate and measure, but they showed high defect densities and a significant amount of oxidation. Nonetheless, the impurities in the CVD-grown samples are led to strong light-dependent charging behaviors and even long-term charge storage within the WS_2 flakes. These properties, though unexpected, may lead to a variety of interesting optoelectronic applications and should be investigated further to see if they can be reproduced in a controlled fashion.

Overall, the optically pumped AFM system provides a unique, spatially localized method for measuring optical nonlinearities that shows a lot of potential for characterizing interesting materials and the role of defects in their nonlinear properties.

4.2 Outlook

In terms of future work on this project, there are three main avenues that could and should be explored.

Firstly, this technique is very promising when it comes to extracting the nonlinear optical properties of 2D materials and structures, such as horizontal heterostructures. However, in order to efficiently perform such measurements, it will first be necessary to find a

better method of locating specific spots on the sample while under UHV conditions. One potential avenue for this will be to use the scanning electron microscope (SEM) that is built into the JEOL measurement chamber to position the tip in the correct location.

Secondly, the UHV, optically-pumped AFM system could be useful for further understanding the oxidation and photo-charging properties of CVD-grown WS_2 monolayers. Since it is believed that these materials undergo photo-oxidation in ambient conditions [42], it is conceivable that one might control the oxidation process by controlling the amount of oxygen and light in the sample environment. By starting with pure, CVD-grown WS_2 and leaking small amounts of oxygen into the UHV chamber while illuminating the sample, one could control the oxidation of the flakes and better understand the charge storage mechanisms observed in this work. Of course, to achieve this experiment, it will first be necessary to obtain monolayer WS_2 flakes that remain pure after long-distance transport.

Finally, there is still a lot of promising work to be done when it comes to improving and optimizing the measurement technique itself. For one, it would be useful to compare a few different samples with well-known susceptibilities in order to systematically extract $\chi^{(2)}$ quantitatively. In addition, one could use a more complex pump-probe scheme similar to electric field induced second harmonic generation (E-FISH) to see how the nonlinear properties of the material change over time. This would involve pumping the material optically and then running an autocorrelation measurement to extract the magnitude of the susceptibility of the material in response to the pump. The delay between the pump and the autocorrelation could then be tuned to extract time-dependent susceptibilities.

Lastly, Equation 2.5 shows that when a material is exposed to both an optical, oscillating electric field and a constant, DC field, the induced polarization is dependent on both fields. Specifically, the zero-frequency polarization (which is relevant for this experiment) is related to the square of the DC field and the square of the optical field by $\chi^{(2)}$ such that,

$$P_{0\omega} = \epsilon_0 \chi^{(1)} E_{DC} + \epsilon_0 \chi^{(2)} E_{DC}^2 + \frac{1}{2} \epsilon_0 \chi^{(2)} E_0^2. \tag{4.1}$$

Thus, even in the absence of an optical field, the polarization induced by sufficiently large DC electric fields is proportional to $\chi^{(2)}$ of the material. One can then imagine using this proportionality to extract the nonlinear optical susceptibility of a material without the need for any optical excitation at all. This scheme could be feasible in an AFM due to the small length scales, since even a small voltage applied over a few nanometers yields a large electric field per area. The AFM also lends itself well to this kind of measurement, due to the wide variety of modulation techniques that are already applied in these microscopes.

In all, there are many promising avenues to explore when it comes to the optically pumped AFM experiment, not only in terms of specific materials to measure, but also in terms of new properties to extract and new measurement schemes to develop.

Appendices

Appendix A

Nonlinear Optical Susceptibilities

MoS_2					
$\chi^{(2)}_{bulk}$ [pm/V]	λ [nm]	First Author	Exciton	Sample Type	Substrate
430	1600	Zhou 2015 [44]		CVD	
5	1560	Autere 2018 [45]		Mech Ex.	285 nm SiO2 on Si
5	1560	Le 2017 [46]		CVD	300 nm SiO2/Si
34	1560	Woodward 2017 [47]		CVD	300 nm SiO2/Si
29	1560	Woodward 2017 [47]		CVD	glass
2	1560	Karvonen 2017 [48]		CVD	SiO2/Si
2	1560	Säynätjoki 2017 [49]		Mech Ex.	Si + 285 nm SiO2
6	1560	Clark 2015 [29]		CVD	300 nm SiO2/Si
40	1350	Clark 2015 [29]	A	CVD	300 nm SiO2/Si
40	1350	Le 2017 [46]	A	CVD	300 nm SiO2/Si
71	1305	Lafeta 2021 [50]	A	CVD	fused quartz
18000	1300	Wang 2020 [27]	A/B	Mech Ex.	285 nnm SiO2/Si
25	1250	Le 2017 [46]	B	CVD	300 nm SiO2/Si
40	1240	Clark 2015 [29]	B	CVD	300 nm SiO2/Si
215	1240	Bredillet 2020 [51]	B	Liquid Ex.	suspension
43	1209	Lafeta 2021 [50]	B	CVD	fused quartz
123	885	Malard 2013 [25]	C	Mech Ex.	300 nm SiO2/Si
250	870	Bredillet 2020 [51]	C	Liquid Ex.	suspension
321	810	Li 2013 [39]	C	Mech Ex.	fused silicon
100000	810	Kumar 2013 [5]		Mech Ex.	90 nm Si/SiO2

Table A.1: MoS_2 $\chi^{(2)}$ literature values

WS_2					
$\chi^{(2)}_{bulk}$ **[pm/V]**	λ **[nm]**	**First Author**	**Exciton**	**Sample Type**	**Substrate**
16.2	1560	Autere 2018 [45]		Mech Ex. (PDMS)	285 nm SiO2 on Si
250	1250	Bredillet 2020 [51]	A	Liquid Ex.	suspension
60.00	1240	Lafeta 2021 [50]	A	CVD	fused quartz
17.14	1200	Lafeta 2021 [50]		CVD	fused quartz
150	1150	Weismann 2016 [33]			
370	1064	Bredillet 2020 [51]	B	Liquid Ex.	suspension
270	1064	Bredillet 2020 [51]	B	Liquid Ex.	suspension
530	1064	Bredillet 2020 [51]	B	Liquid Ex.	suspension
250	1040	Bredillet 2020 [51]	B	Liquid Ex.	suspension
680	880	Fan 2017 [52]	C	CVD (Spiral)	SiO2
400	850	Weismann 2016 [33]	C/D		
9000	832	Janisch 2014 [31]	C/D	CVD	suspension
8920	832	Janisch 2014 [31]	C/D	CVD	300 nm SiO2 on Si
500	832	Janisch 2014 [31]	C/D		
870	825	Bredillet 2020 [51]	C/D	Liquid Ex.	suspension
1.66*MoS_2	800	Mennel 2019 [53]	C/D	Mech. Ex.	5 μm PEN/SU-8
1140	600	Weismann 2016 [33]			
850	580	Weismann 2016 [33]			
125	500	Weismann 2016 [33]			

Table A.2: WS_2 $\chi^{(2)}$ literature values.

Appendix B

WS_2 Exciton Energies

Exciton	Energy	Wavelength	Source
A	2.01	616.82	Lafeta [50]
	2.03	610	Autere [45]
	1.98	626.16	Zeng [54]
	2.02	613.76	Zhu [55]
	1.94	640	Fan [52]
B	2.34	530	Autere [45]
	2.38	520.92	Zeng [54]
	2.4	516.58	Zhu [55]
	2.34	530	Fan [52]
C	2.8	442.79	Zhu [55]
	2.64	470	Fan [52]
D	2.88	430	Fan [52]
Trion	1.96	632.55	Lafeta [50]
	1.57	790	Autere [45]

Table B.1: WS_2 exciton energy values

Appendix C

X-Ray Photoelectron Spectroscopy

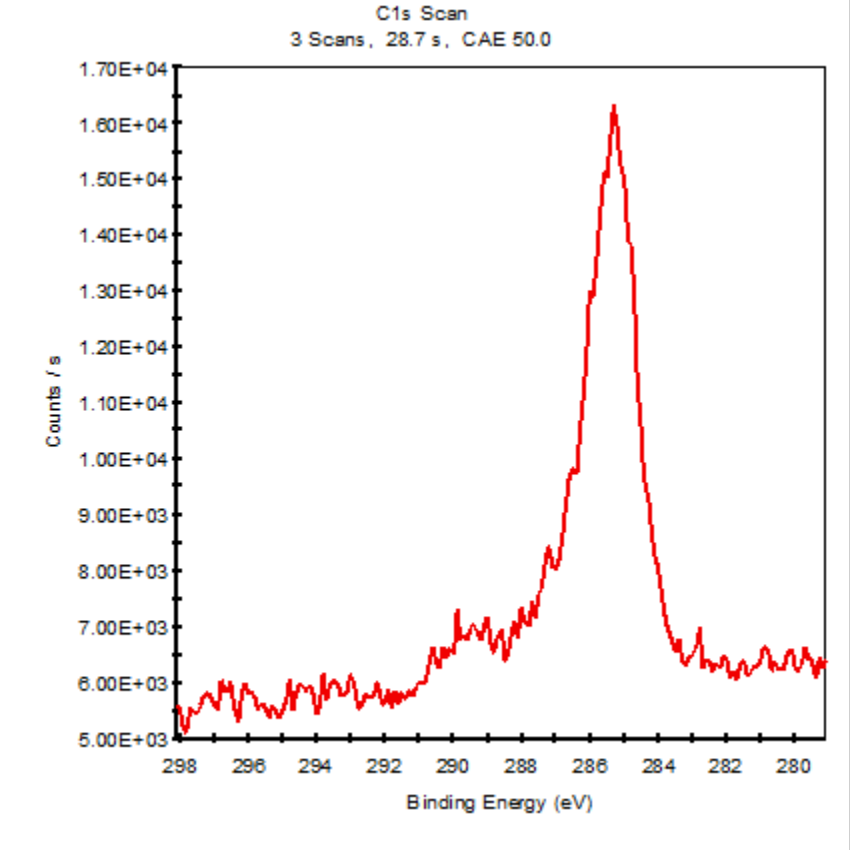

Figure C.1: XPS carbon scan of CVD-grown WS_2 flakes. The spectrum shows a small amount of charging, about 0.75eV, since the peak falls at 285.54eV while that uncharged CS1 peak is expected to occur at 284.8eV [56]. This data was taken using an Al K Alpha source gun with spot size of $400\mu m$.

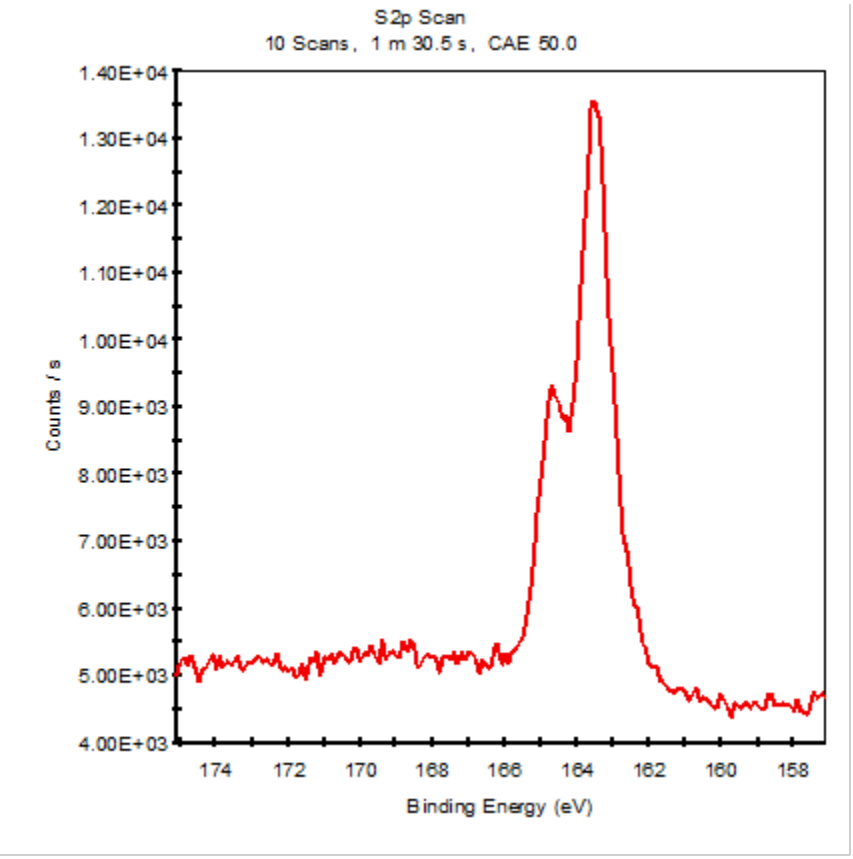

Figure C.2: Sulphur scan of x-ray photoelectron spectrum of CVD-grown WS_2 flakes. This data was taken using an Al K Alpha source gun with spot size of $400\mu m$.

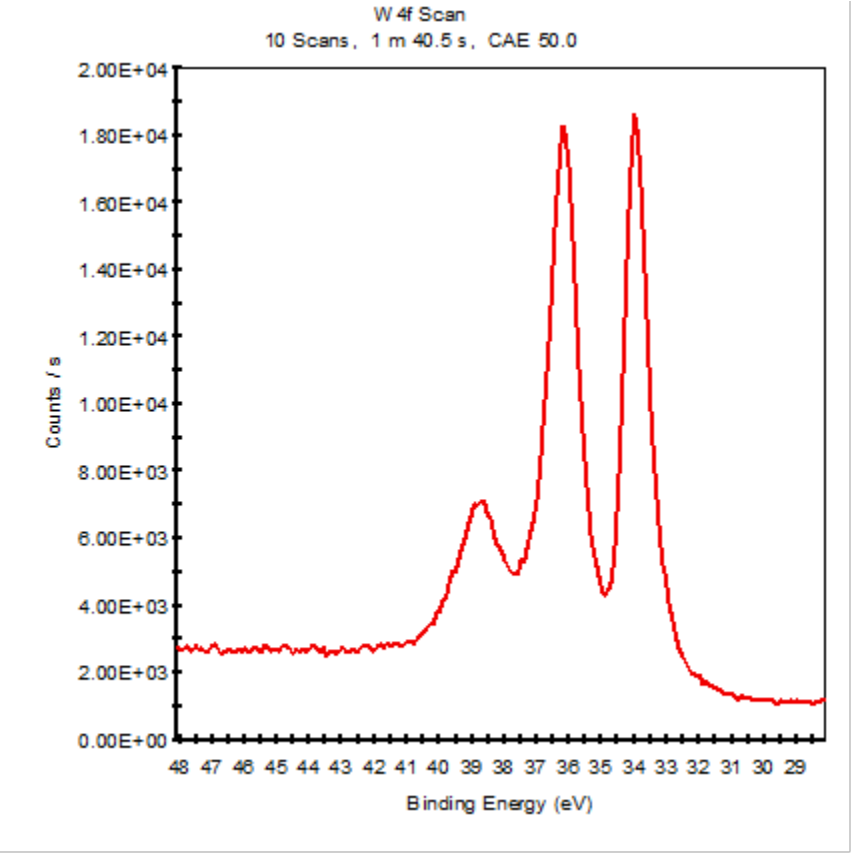

Figure C.3: Tungsten scan of x-ray photoelectron spectrum of CVD-grown WS_2 flakes. The shoulder around 33eV is indicative of some WS_2 within the scan depth of measurement, though the spectrum is dominated by partially oxidizes WO_2. This data was taken using an Al K Alpha source gun with spot size of $400\mu m$.

Name	Peak BE	FWHM eV	Area (P) CPS.eV	Atomic %
O1s	531.93	2.78	1993837.74	48.47
Al2p	75.15	2.68	345205.03	31.99
W4f	35.45	4.98	417266.87	1.92
S2p	164.03	2.96	134751.09	3.91
C1s	285.54	1.77	202949.88	11.93
Na1s	1072.22	2.67	105268.83	1.27
N1s	401.53	2.39	13528.62	0.51

Table C.1: Elemental quantification of XPS spectrum shown in Figure 3.5. The binding energies are taken as the average peak positions for each element, even when elements display multiple peaks.

Bibliography

[1] K. S. Novoselov, A. K. Geim, S. V. Morozov, D. Jiang, Y. Zhang, S. V. Dubonos, I. V. Grigorieva, and A. A. Firsov, "Electric Field Effect in Atomically Thin Carbon Films," vol. 306, no. October, pp. 666–670, 2004.

[2] K. Khan, A. K. Tareen, M. Aslam, R. Wang, Y. Zhang, A. Mahmood, Z. Ouyang, H. Zhang, and Z. Guo, *Recent developments in emerging two-dimensional materials and their applications*, vol. 8. Royal Society of Chemistry, 2020.

[3] W. Choi, N. Choudhary, G. H. Han, J. Park, D. Akinwande, and Y. H. Lee, "Recent development of two-dimensional transition metal dichalcogenides and their applications," *Materials Today*, vol. 20, no. 3, pp. 116–130, 2017.

[4] Q. H. Wang, K. Kalantar-Zadeh, A. Kis, J. N. Coleman, and M. S. Strano, "Electronics and optoelectronics of two-dimensional transition metal dichalcogenides," *Nature Nanotechnology*, vol. 7, no. 11, pp. 699–712, 2012.

[5] N. Kumar, S. Najmaei, Q. Cui, F. Ceballos, P. M. Ajayan, J. Lou, and H. Zhao, "Second harmonic microscopy of monolayer MoS2," *Physical Review B - Condensed Matter and Materials Physics*, vol. 87, no. 16, pp. 1–6, 2013.

[6] L. Zhou, H. Fu, T. Lv, C. Wang, H. Gao, D. Li, L. Deng, and W. Xiong, "Nonlinear optical characterization of 2d materials," *Nanomaterials*, vol. 10, no. 11, pp. 1–38, 2020.

[7] A. Castellanos-Gomez, "Why all the fuss about 2D semiconductors?," *Nature Photonics*, vol. 10, no. 4, pp. 202–204, 2016.

[8] D. W. Latzke, W. Zhang, A. Suslu, T. R. Chang, H. Lin, H. T. Jeng, S. Tongay, J. Wu, A. Bansil, and A. Lanzara, "Electronic structure, spin-orbit coupling, and interlayer interaction in bulk MoS2 and WS2," *Physical Review B - Condensed Matter and Materials Physics*, vol. 91, no. 23, pp. 1–6, 2015.

[9] R. W. Boyd, *Nonlinear Optics*. Academic Press, 3rd ed., mar 2008.

[10] Z. Schumacher, A. Spielhofer, Y. Miyahara, and P. Grutter, "The limit of time resolution in frequency modulation atomic force microscopy by a pump-probe approach," *Applied Physics Letters*, vol. 110, no. 5, 2017.

[11] Z. Schumacher, R. Rejali, R. Pachlatko, A. Spielhofer, P. Nagler, Y. Miyahara, D. G. Cooke, and P. Grütter, "Nanoscale Force Sensing of an Ultrafast Nonlinear Optical Response," *Proceedings of the National Academy of Sciences of the United States of America*, vol. 117, no. 33, pp. 19773–19779, 2020.

[12] L. Gross, F. Mohn, N. Moll, P. Liljeroth, and G. Meyer, "The chemical structure of a molecule resolved by atomic force microscopy," *Science*, vol. 325, no. 5944, pp. 1110–1114, 2009.

[13] F. J. Giessibl, "Advances in atomic force microscopy," vol. 75, no. July, 2003.

[14] Y. Seo and W. Jhe, "Atomic force microscopy and spectroscopy," *Reports on Progress in Physics*, vol. 71, no. 1, 2008.

[15] R. García and R. Pérez, *Dynamic atomic force microscopy methods*, vol. 47. 2002.

[16] U. Zerweck, C. Loppacher, T. Otto, S. Grafström, and L. M. Eng, "Accuracy and resolution limits of Kelvin probe force microscopy," no. March, pp. 1–9, 2005.

[17] D. Rompotis, "A Single-shot Nonlinear Autocorrelation Approach for Time-Resolved Physics in the Vacuum Ultraviolet Spectral Range," 2015.

[18] R. Trebino and E. Zeek, "The Autocorrelation, the Spectrum, and Phase Retrieval," in *Frequency-Resolved Optical Gating: The Measurement of Ultrashort Laser Pulses*, ch. 4, pp. 61–99, New York, NY: Springer US, 1 ed., 2000.

[19] D. J. Griffiths, "Electric Fields in Matter," in *Introduction to Electrodynamics*, ch. 4, pp. 167–209, Cambridge: Cambridge University Press, 4th ed., jun 2017.

[20] R. Rejali, *Ultrafast Atomic Force Microscopy*. PhD thesis, McGill University, 2018.

[21] Z. Schumacher, "Time-domain Kelvin Probe Force Microscopy for Local Ultra-Fast Decay Time Measurements Thesis by Zeno Schumacher," *PhD thesis*, no. June, 2016.

[22] A. J. Kyn, N. Humber, D. Hertel, K. Meerholz, and M. Sokolowitski, "A highly ordered commensurate structure of merocyanine tetramers on Ag(100): STM- and SPA-LEED-investigations," 2020.

[23] H. Bürckstümmer, E. V. Tulyakova, M. Deppisch, M. R. Lenze, N. M. Kronenberg, M. Gsänger, M. Stolte, K. Meerholz, and F. Würthner, "Efficient solution-processed bulk heterojunction solar cells by antiparallel supramolecular arrangement of dipolar donor-acceptor dyes," *Angewandte Chemie - International Edition*, vol. 50, no. 49, pp. 11628–11632, 2011.

[24] N. Gildemeister, G. Ricci, L. Böhner, J. M. Neudörfl, D. Hertel, F. Würthner, F. Negri, K. Meerholz, and D. Fazzi, "Understanding the structural and charge transport property relationships for a variety of merocyanine single-crystals: A bottom up computational investigation," *Journal of Materials Chemistry C*, vol. 9, no. 33, pp. 10851–10864, 2021.

[25] L. M. Malard, T. V. Alencar, A. P. M. Barboza, K. F. Mak, and A. M. De Paula, "Observation of intense second harmonic generation from MoS2 atomic crystals," *Physical Review B - Condensed Matter and Materials Physics*, vol. 87, no. 20, pp. 1–5, 2013.

[26] M. Cowie, R. Plougmann, Z. Schumacher, and P. Grutter, "Single-dopant band bending fluctuations in MoSe2 measured with electrostatic force microscopy," *Physical Review Materials*, 2022.

[27] Y. Wang, M. Ghotbi, S. Das, Y. Dai, S. Li, X. Hu, X. Gan, J. Zhao, and Z. Sun, "Difference frequency generation in monolayer MoS2," *Nanoscale*, vol. 12, pp. 19638–19643, oct 2020.

[28] D. J. Clark, V. Senthilkumar, C. T. Le, D. L. Weerawarne, B. Shim, J. I. Jang, J. H. Shim, J. Cho, Y. Sim, M. J. Seong, S. H. Rhim, A. J. Freeman, K. H. Chung, and Y. S. Kim, "Strong optical nonlinearity of CVD-grown MoS2 monolayer as probed by wavelength-dependent second-harmonic generation," *Physical Review B - Condensed Matter and Materials Physics*, vol. 90, no. 12, pp. 1–5, 2014.

[29] D. J. Clark, V. Senthilkumar, C. T. Le, D. L. Weerawarne, B. Shim, J. I. Jang, J. H. Shim, J. Cho, Y. Sim, M. J. Seong, S. H. Rhim, A. J. Freeman, K. H. Chung, and Y. S. Kim, "Erratum: Strong optical nonlinearity of CVD-grown MoS2 monolayer as probed by wavelength-dependent second-harmonic generation (Physical Review B - Condensed Matter and Materials Physics (2014) R:90 (121409))," *Physical Review B - Condensed Matter and Materials Physics*, vol. 92, no. 15, pp. 2014–2015, 2015.

[30] W. Zhao, Z. Ghorannevis, L. Chu, M. Toh, C. Kloc, P.-H. Tan, and G. Eda, "Evolution of Electronic Structure in Atomically Thin Sheets of WS2 and WSe2," *ACS Nano*, vol. 7, no. 1, pp. 791–797, 2013.

[31] C. Janisch, Y. Wang, D. Ma, N. Mehta, A. L. Elías, N. Perea-López, M. Terrones, V. Crespi, and Z. Liu, "Extraordinary Second Harmonic Generation in Tungsten Disulfide Monolayers," *Scientific Reports 2014 4:1*, vol. 4, pp. 1–5, jul 2014.

[32] O. A. Shamir, *Broadband Electrooptic Modulators Based on Gallium Arsenide Materials*. PhD thesis, Massachusetts Institute of Technology, 2012.

[33] M. Weismann and N. C. Panoiu, "Theoretical and computational analysis of second- and third-harmonic generation in periodically patterned graphene and transition-metal dichalcogenide monolayers," *Physical Review B*, vol. 94, no. 3, 2016.

[34] S. L. Wong, H. Liu, and D. Chi, "Recent progress in chemical vapor deposition growth of two-dimensional transition metal dichalcogenides," *Progress in Crystal Growth and Characterization of Materials*, vol. 62, no. 3, pp. 9–28, 2016.

[35] M. Chubarov, T. H. Choudhury, D. R. Hickey, S. Bachu, T. Zhang, A. Sebastian, A. Bansal, H. Zhu, N. Trainor, S. Das, M. Terrones, N. Alem, and J. M. Redwing, "Wafer-Scale Epitaxial Growth of Unidirectional WS2 Monolayers on Sapphire," *ACS Nano*, vol. 15, no. 2, pp. 2532–2541, 2021.

[36] K. S. Novoselov, D. Jiang, F. Schedin, T. J. Booth, V. V. Khotkevich, S. V. Morozov, and A. K. Geim, "Two-dimensional atomic crystals," *Proceedings of the National Academy of Sciences of the United States of America*, vol. 102, no. 30, pp. 10451–10453, 2005.

[37] X. Cao, C. Jiang, D. Tan, Q. Li, S. Bi, and J. Song, "Recent mechanical processing techniques of two-dimensional layered materials: A review," *Journal of Science: Advanced Materials and Devices*, vol. 6, no. 2, pp. 135–152, 2021.

[38] S. Roddaro, P. Pingue, V. Piazza, V. Pellegrini, and F. Beltram, "The optical visibility of graphene: Interference colors of ultrathin graphite on SiO2," *Nano Letters*, vol. 7, no. 9, pp. 2707–2710, 2007.

[39] H. Li, J. Wu, X. Huang, G. Lu, J. Yang, X. Lu, Q. Xiong, and H. Zhang, "Rapid and reliable thickness identification of two-dimensional nanosheets using optical microscopy," *ACS Nano*, vol. 7, no. 11, pp. 10344–10353, 2013.

[40] K. F. Mak, C. Lee, J. Hone, J. Shan, and T. F. Heinz, "Atomically thin MoS2: A new direct-gap semiconductor," *Physical Review Letters*, vol. 105, p. 136805, sep 2010.

[41] J. O. Carlsson and P. M. Martin, *Chemical Vapor Deposition*. Elsevier Ltd., third edit ed., 2010.

[42] J. C. Kotsakidis, Q. Zhang, A. L. Vazquez De Parga, M. Currie, K. Helmerson, D. K. Gaskill, and M. S. Fuhrer, "Oxidation of Monolayer WS2 in Ambient Is a Photoinduced Process," *Nano Letters*, vol. 19, no. 8, pp. 5205–5215, 2019.

[43] A. Bansal, M. Hilse, B. Huet, K. Wang, A. Kozhakhmetov, J. H. Kim, S. Bachu, N. Alem, R. Collazo, J. A. Robinson, R. Engel-Herbert, and J. M. Redwing, "Substrate modification during chemical vapor deposition of hBN on sapphire," *ACS Applied Materials and Interfaces*, vol. 13, no. 45, pp. 54516–54526, 2021.

[44] X. Zhou, J. Cheng, Y. Zhou, T. Cao, H. Hong, Z. Liao, S. Wu, H. Peng, K. Liu, and D. Yu, "Strong Second-Harmonic Generation in Atomic Layered GaSe," *Journal of the American Chemical Society*, vol. 137, no. 25, pp. 7994–7997, 2015.

[45] A. Autere, H. Jussila, A. Marini, J. R. Saavedra, Y. Dai, A. Säynätjoki, L. Karvonen, H. Yang, B. Amirsolaimani, R. A. Norwood, N. Peyghambarian, H. Lipsanen, K. Kieu, F. J. G. De Abajo, and Z. Sun, "Optical harmonic generation in monolayer group-VI transition metal dichalcogenides," *Physical Review B*, vol. 98, no. 11, pp. 1–7, 2018.

[46] C. T. Le, D. J. Clark, F. Ullah, J. I. Jang, V. Senthilkumar, Y. Sim, M. J. Seong, K. H. Chung, J. W. Kim, S. Park, S. H. Rhim, G. Kim, and Y. S. Kim, "Impact of selenium doping on resonant second-harmonic generation in monolayer MoS2," *ACS Photonics*, vol. 4, no. 1, pp. 38–44, 2017.

[47] R. I. Woodward, R. T. Murray, C. F. Phelan, R. E. De Oliveira, T. H. Runcorn, E. J. Kelleher, S. Li, E. C. De Oliveira, G. J. Fechine, G. Eda, and C. J. De Matos, "Characterization of the second- and third-order nonlinear optical susceptibilities of monolayer MoS2 using multiphoton microscopy," *2D Materials*, vol. 4, no. 1, 2017.

[48] L. Karvonen, A. Säynätjoki, M. J. Huttunen, A. Autere, B. Amirsolaimani, S. Li, R. A. Norwood, N. Peyghambarian, H. Lipsanen, G. Eda, K. Kieu, and Z. Sun, "Rapid visualization of grain boundaries in monolayer MoS2 by multiphoton microscopy," *Nature Communications*, vol. 8, pp. 1–8, 2017.

[49] A. Säynätjoki, L. Karvonen, H. Rostami, A. Autere, S. Mehravar, A. Lombardo, R. A. Norwood, T. Hasan, N. Peyghambarian, H. Lipsanen, K. Kieu, A. C. Ferrari, M. Polini, and Z. Sun, "Ultra-strong nonlinear optical processes and trigonal warping in MoS2 layers," *Nature Communications*, vol. 8, no. 1, pp. 1–8, 2017.

[50] L. Lafeta, A. Corradi, T. Zhang, E. Kahn, I. Bilgin, B. R. Carvalho, S. Kar, M. Terrones, and L. M. Malard, "Second- and third-order optical susceptibilities in bidimensional semiconductors near excitons states," pp. 1–8, 2021.

[51] K. Bredillet, J. Riporto, G. T. Forcherio, J. R. Dunklin, J. P. Wolf, L. Bonacina, Y. Mugnier, and R. Le Dantec, "Dispersion of the nonlinear susceptibility of MoS2 and WS2 from second-harmonic scattering spectroscopy," *Physical Review B*, vol. 102, no. 23, pp. 1–7, 2020.

[52] X. Fan, Y. Jiang, X. Zhuang, H. Liu, T. Xu, W. Zheng, P. Fan, H. Li, X. Wu, X. Zhu, Q. Zhang, H. Zhou, W. Hu, X. Wang, L. Sun, X. Duan, and A. Pan, "Broken Symmetry Induced Strong Nonlinear Optical Effects in Spiral WS2 Nanosheets," *ACS Nano*, vol. 11, no. 5, pp. 4892–4898, 2017.

[53] L. Mennel, M. Paur, and T. Mueller, "Second harmonic generation in strained transition metal dichalcogenide monolayers: MoS 2 , MoSe 2 , WS 2 , and WSe 2," *APL Photonics*, vol. 4, no. 3, 2019.

[54] H. Zeng, G. B. Liu, J. Dai, Y. Yan, B. Zhu, R. He, L. Xie, S. Xu, X. Chen, W. Yao, and X. Cui, "Optical signature of symmetry variations and spin-valley coupling in atomically thin tungsten dichalcogenides," *Scientific Reports*, vol. 3, pp. 2–6, 2013.

[55] B. Zhu, X. Chen, and X. Cui, "Exciton binding energy of monolayer WS2," *Scientific Reports*, vol. 5, 2015.

[56] F. De, H. E. Feng, X. I. E. Junlin, and X. U. E. Lihui, "Calibration of Binding Energy Positions with C1s for XPS Results," pp. 711–718, 2020.